Chapter 3

# The HXDS Flow Proportional Counters

*Brad Wargelin and Richard J. Edgar*

## 3.1 Introduction

In this chapter we discuss the calibration of the seven Flow Proportional Counters (FPCs) used during AXAF ground calibration. Five of the FPCs served as Beam Normalization Detectors (BNDs) throughout both phases of AXAF calibration, and one (with a backup) was used in the telescope focal plane in combination with a set of apertures to measure the point response functions and effective areas of the AXAF mirrors and transmission gratings during Phase 1 calibration. The BNDs also served as references for determining the effective areas of the several telescope/grating/flight-detector combinations.

An overview of the entire HXDS, along with a detailed discussion of the design and operation of the FPCs, may be found in Wargelin et al. (1997). In case of any discrepancies regarding distances and dimensions, this calibration report takes precedence.

### 3.1.1 Calibration Overview

The FPC calibration program was based on characterization of individual components (such as window transmission and aperture size) and the calibration of complete detector systems, particularly with regard to their relative and absolute quantum efficiencies. Calibration was conducted at SAO (primarily on the HXDS X-ray Pipe Facility), at MSFC (primarily during Phase I and J Flat Field testing at the XRCF in May and June 1997), and in collaboration with the Physikalisch-Technische Bundesanstalt (PTB) at the BESSY synchrotron in Berlin, Germany (December 1997 and January 1998). Theoretical modeling was also employed to quantify small effects that would be too difficult to measure directly. A summary of the calibration program is provided in Table 3.1.

## 3.2 Apertures

### 3.2.1 Focal Plane Apertures

#### Optical and X-ray Measurements

For apertures larger than about 100 $\mu$m, areas can be measured with sufficient accuracy using an optical microscope and two-dimensional translation stage. Although all apertures were measured





| Characteristic | Measurement | Where |
|---|---|---|
| Focal plane aperture sizes | For smallest apertures, use electron microscope and/or measure relative sizes with uniform x-ray beam. | SAO BESSY white |
| | For larger apertures, use optical microscope with 2d stages. | SAO |
| BND aperture sizes | Optical microscope, with most accurate measurements for fpc_hn and fpcx2 blocking plates. | SAO |
| | Net collecting areas of other BNDs are normalized to fpc_hn by flat field relative QE measurements. | XRCF |
| Window support wire blockage | Calculate based on nominal wire diameter and do in/out x-ray measurements. | SAO |
| Gain nonuniformity | 1d scan of several FPCs | SAO BESSY SX700 |
| Anode aging | 1d scan of fpc_x2 and fpc_hn | XRCF BESSY SX700 |
| Spectral response function | Use monochromatic beam | BESSY SX700 KMC |
| QE: window transmission | In/out tests | BESSY SX700 |
| QE: relative | Cross-calibrate all FPCs and SSDs during Phases I and J | XRCF |
| QE: absolute | Compare FPC rate with calibrated monochromator beam intensity, as part of Spectral Response Function msmts | BESSY SX700 |
| QE: absolute broadband | Use synchrotron white beam with calibrated filters and compare FPC rate with calculated beam intensity | BESSY white |
| QE: gas opacity | Vary gas pressure at 1700 eV. | BESSY SX700 |
| | Scan across Ar-K edge at 3206 eV. | BESSY KMC |
| QE: window bowing | Fine-scale scans at 330,500,930 eV | BESSY SX700 |
| QE: window nonuniformity | XRCF relative QEs are for whole windows but BESSY beams are small. Sample QE at many points to relate XRCF to BESSY. | BESSY SX700 |
| Deadtime consistency | Test rate reproducibility with SSD and $^{55}$Fe, using many pulser rates, LLD settings, shaping times. | SAO lab |
| Counting rate linearity | Compare deadtime-corrected FPC relative counting rates with precisely known relative beam intensity | BESSY SX700 BESSY white |
| Misc. small effects | Model effects of temperature, pressure, effective gas and window absorption path lengths, anode wire absorption, aperture transparency at high energies, focussed x-rays hitting fpc_x2 support wires, window support wire reflectivity. | SAO |

Table 3.1: Summary of the FPC calibration program.

before AXAF calibration, several of the most important were measured again with greater care in April 1998. Each of those apertures, between 100 and 500 $\mu$m in diameter, was measured twice along four diameters, with calibrated gauge blocks to correct for microscope stage errors (which were extremely small). The measurement resolution limit was 2.5 $\mu$m, and average diameters are quoted to the nearest 0.5 $\mu$m. Error estimates are equal to the larger of the resolution and the "sample standard deviation," defined as

$$\left( \frac{\sum_{i=1}^{N} (X_i - \langle X \rangle)^2}{N-1} \right)^{1/2}$$

where $N$ is the number of diameters measured. (Strictly speaking, the sample standard deviation is not applicable here, but it provides a means of quantifying the uncertainty in the effective diameter of each aperture.) The two readings for each measurement were averaged and nearly always differed by $\pm 2.5$ $\mu$m or less, so the average was treated as one value and $N = 4$. All the holes were quite circular except for the 300-$\mu$m, which had a sample standard deviation of 5.5 $\mu$m; because that hole is irregular and we may not have measured a sufficiently representative sample of diameters, we estimate the uncertainty in its average diameter as $\pm 4$ $\mu$m.

Aperture sizes are listed in Table 3.2. Note that for the remeasured apertures, the original quoted uncertainties were sometimes too small. For the larger apertures (larger than 500 $\mu$m), the original uncertainties were $\pm 12.5$ $\mu$m; the uncertainties listed in the table have been subjectively increased because only one or two diameters were measured, etc. Because the HRMA PRF is so peaked, however, errors in the sizes of these larger apertures cause negligible errors in Effective Area and Encircled Energy measurements.

For apertures smaller than 100 $\mu$m, sizes are most accurately measured with electron microscopes and calibrated references, or by measuring relative aperture areas by comparing counting rates when the apertures are exposed to a uniform x-ray beam. When using an electron microscope, measuring the size of the smallest apertures is complicated by the fact that the hole size becomes comparable to or smaller than the thickness of the gold foil in which it resides; the microscope can only "see" the entrance side of the tunnel, which is generally flared, and so it becomes problematic to assign a single number to describe the size of a hole that varies with depth, particularly when it is used with a focussed x-ray beam.

For these small apertures, therefore, we attempted to make measurements of relative size at the BESSY synchrotron, exposing the apertures to a nearly flat white beam and recording the observed x-ray signal with a photodiode. Because of alignment problems, however, some and perhaps all of the apertures were partially blocked from the beam, and so we must rely on the electron microscope results. (Future analysis of the BESSY results may provide useful results.) We were able, however, to confirm that the effective size of the nominal 5-$\mu$m-diameter aperture is much smaller than expected, as was observed during HMRA calibration at the XRCF.

**Aperture Transparency**

In order to minimize errors arising from the "tunnel" effect, apertures smaller than 25 $\mu$m were fabricated in thinner gold foil, i.e., 12.5 vs. 40-$\mu$m or thicker for larger apertures. (An exception is the 5-$\mu$m aperture, made from 40-$\mu$m foil. It replaced the original, too-small 5-$\mu$m aperture made from 12.5-$\mu$m foil during the calibration rehearsal phase.) At energies above about 6 keV the thin foil becomes increasingly transparent to x-rays (using the 1995 Henke tables and assuming a density of 18.85 g/cm$^3$, transmission equals 1.49e-6 at 5415 eV, 1.34e-4 at 6404 eV, 0.00307 at 7478 eV, 0.00831 at 8048 eV, 0.0184 at 8639 eV, and 0.0644 at 10 keV) and since the fraction of x-rays





| Aperture | Shape | Nominal Size ($\mu$m) | Measured Size ($\mu$m) | Accuracy ($\pm\mu$m) |
|---|---|---|---|---|
| A | circle | 35000 diam | 35010 | 40 |
| B | circle | 20000 diam | 20000 | 30 |
| C | circle | 10000 diam | 10020 | 20 |
| D | circle | 4000 diam | 4000 | 15 |
| E | circle | 2000 diam | 1990 | 15 |
| F | circle | 1000 diam | 980 | 15 |
| G | circle | 500 diam | 500<br>498.0 (new) | 2.5<br>2.5 |
| H | circle | 300 diam | 300<br>285.5 (new) | 2.5<br>4.0 |
| I | circle | 200 diam | 200<br>195.5 (new) | 2.5<br>2.5 |
| J | circle | 150 diam | 150<br>149.5 (new) | 2.5<br>2.5 |
| K | circle | 100 diam | 101<br>99.0 (new) | 2.5<br>2.5 |
| L | circle | 70 diam | 70 | 4 |
| M | circle | 50 diam | 49 | 3 |
| N | circle | 40 diam | 40 | 3 |
| O | circle | 30 diam | 30 | 2 |
| P | circle | 20 diam | 20 | 2 |
| Q | circle | 15 diam | 15 | 3 |
| R | circle | 10 diam | 10 | 2 |
| S | circle | 7.5 diam | 7.5 | 2 |
| T | circle | 5* diam | 3 | 1 |
| U | circle | 3 diam | 3 | 1 |
| V | slit, vertical | 5 × 100 | 5 × 100 | 2.5, 2.5 |
| W | slit, vert−5° | 5 × 100 | 5 × 100 | 2.5, 2.5 |
| X | slit, vert+5° | 5 × 100 | 6 × 100 | 2.5, 2.5 |
| Y | slit, horiz−15° | 5 × 100 | 6 × 98 | 2.5, 2.5 |
| Z | slit, vert−15° | 5 × 100 | 5 × 98 | 2.5, 2.5 |
| AA | slit, vertical | 10 × 200 | 10 × 198 | 2.5, 2.5 |
| AB | slit, vert−5° | 10 × 200 | 10 × 200 | 2.5, 2.5 |
| AC | slit, vert+5° | 10 × 200 | 10 × 198 | 2.5, 2.5 |
| AD | slit, horizontal | 10 × 200 | 10 × 198 | 2.5, 2.5 |
| AE | slit, vertical | 80 × 500 | 80 × 500 | 2.5, 2.5 |
| AF | slit, vertical | 500 × 10000 | 500 × 9990 | 2.5, 25 |
| AG | slit, vert+5° | 500 × 10000 | 506 × 10010 | 2.5, 25 |
| AH | slit, vert−5° | 500 × 10000 | 500 × 10020 | 2.5, 25 |

Table 3.2: Focal plane aperture sizes. Slit orientation: looking from the XSS, positive angles are clockwise. Circular apertures larger than 500 $\mu$m are made from 1/8"-thick stainless steel. The four largest slits and the 30-500 $\mu$m circles are laser-drilled in 40-$\mu$m gold foil. Smaller circles and slits are fabricated in 12.5-$\mu$m gold foil by ion beam milling. (*The 5-$\mu$m circle is made from 40-$\mu$m foil.)

focussed on the aperture hole is quite small at high energies because of scattering, a significant fraction of the detected x-rays may be transmitted through the foil out to a diameter of 2 mm, which is the size of the hole in the stainless steel "cupholder" which holds the foils. The measured Encircled Energy Fraction for an aperture of diameter $D$ is then given by

$$EEF(D)_{meas} = EEF(D)_{true} + [EEF(2mm) - EEF(D)_{true}]\,T$$

where $T$ is the transmission of the gold foil at the energy of the EE measurement (with the approximation that all the x-rays are at the line energy). The true EEF is then

$$EEF(D)_{true} = \frac{EEF(D)_{meas} - EEF(2mm)T}{1-T}.$$

As a worst case example, if the measured EE fraction for HRMA shell1 at Cu-K$\alpha$ is 0.031 with the 10-$\mu$m aperture, and the EEF at 2 mm is 0.82, then $EE(10\mu m)_{meas}/EE(10\mu m)_{true}$ is $0.031/((0.031 - (0.82)(0.00831))/(1 - 0.00831) = 1.27$. At lower energies the corrections (for measurements actually conducted) are much less than 1%, which is completely negligible compared with other uncertainties.

**Support Wire Blockage—the "Mesh" Effect**

Another correction arises from the small fraction of focussed x-rays that hit the wires that support the FPC window. With a perfect mirror, the x-rays from each HRMA shell would intercept the FPC window in rings that fit between the window support wires (just over 1 mm in diameter for shell1, versus the wire pitch of 2 mm), but in the real HRMA, some x-rays are scattered to larger radii. A set of on-axis raytraces was run to quantify this effect and the results are described in great detail in Chapter 6. Corrections are largest for large apertures at high energies, with a value of just over 0.5% for the total HRMA at 8 keV, and 2% for shell 1 by itself. For off-axis sources and grating images, the image centroid will be slightly displaced, but much more important is the fact that the PRF is larger, especially for off-axis measurements. In the worst cases, corrections of a few percent may be needed, but accurate estimates require raytrace analysis.

### 3.2.2 BND Apertures

**Blocking Plate Aperture Size**

In order to determine the effective area of AXAF it is necessary to know the net collecting area of each of the BND FPCs, which is equal to the open area of the window times the effective QE. In practice, the only areas we need to measure are those of the blocking plate apertures for fpc_x2 and fpc_hn since all the other BND FPCs are normalized via the flat field relative QE measurements. For simplicity, and because the variation among them is negligible, the areas for all four rectangular BND-H apertures are defined to be the same, i.e., equal to the area of the full fpc_hn aperture.

Using an optical microscope with calibrated gauge blocks, the dimensions of the fpc_hn and fpc_x2 blocking plate apertures were measured to a resolution of 0.0001" (2.5 $\mu$m), with each measurement made twice (and the average of the two treated as one result). Results are shown in Table 3.3.

Error estimates for the measured values are equal to the sample standard deviation, as defined earlier, and the net area uncertainty is calculated using standard error propagation. The actual area uncertainties are somewhat different (larger if the samples were not representative, smaller if they were), but are essentially negligible if the quoted errors are any indication (0.06% for fpc_x2 and less than 0.03% for fpc_hn).





| Detector/Aperture | Dimension | Number sampled | Value |
|---|---|---|---|
| fpc_hn/full | length | 3 | 98.963 ± 0.016 mm |
| | width | 5 | 36.441 ± 0.006 mm |
| | corner radius | 2 in each corner | 6.314 ± 0.038 mm |
| | area | | 3572.1 ± 0.9 mm$^2$ |
| | net open area for all BND-H FPCs | | **3224 ± 16 mm$^2$** |
| fpc_hn/36 | area ratio vs. full aperture | | 0.2835 ± 0.0003 |
| | net open area | | **914 ± 5 mm$^2$** |
| fpc_x2 | diameter | 4 | 36.784 ± 0.010 mm |
| | area | | 1062.7 ± 0.6 mm$^2$ |
| | net open area | | **959 ± 5 mm$^2$** |

Table 3.3: Blocking plate aperture sizes for reference detectors. The theoretical open area fraction (not blocked by support wires) is 90.26%, assuming 100-$\mu$m-diameter wires.

**Support Wire Blockage**

The major, though still small, source of uncertainty in the net geometric open area of the windows is the fraction blocked by the support wires. These wires are nominally 100-$\mu$m in diameter, with 2-mm pitch, so the calculated blocked area fraction per windowlet is equal to (area of 2 crossed wires - area of wire intersection)/(area of unit cell) = (2 x 2.0mm x 0.1mm - $(0.1\text{mm})^2$)/$(2.0\text{mm})^2$ = 0.0975. When accounting for fractional windowlets and curved edges of the blocking plate apertures, the blocked fraction is actually equal to 0.0974 for fpc_hn and fpc_x2. The number and length of the wires can be easily and accurately determined, so any uncertainty arises from knowing the average wire diameter. Measuring all the wires with a microscope is impractical, so one can either estimate the range of likely diameters (a 10% difference in the wire diameter makes a 0.9% difference in the open area fraction), or experimentally determine the open fraction with an in/out x-ray measurement.

Such measurements were conducted on the SAO Pipe in March 1998 for the fpc_hn and fpc_x2 windows. The fpc_hn (or fpc_x2) blocking plate was mounted on fpc_hb, which was held fixed in the x-ray beam, while the corresponding window was moved in and out in front of the detector. The measurements used Ti-K x-rays from a Manson source with 100- $\mu$m Ti filter, with normalization provided by a VETA monitor counter. The normalized ratio of the in/out counting rates is equal to the fraction of open area between the wires, after making small corrections for absorption by the polyimide/Al window material and the overlap of wires in the test and detector windows.

The statistical uncertainty for the fpc_hn measurement was ±0.12%, but there was a systematic uncertainty of 0.14% because we did not have time to align everything well enough to tell if one of the window support wires was included within the aperture or not. Splitting the difference and strictly adding the statistical and systematic uncertainties, and correcting for window absorption of 0.0056 ± 0.0006, the measured open area fraction was 89.77% of the total area of 3572.1 mm$^2$, or 3206.7 ± 8.6 mm$^2$ (0.27% uncertainty). This is 0.54% smaller than the model which assumes 100-$\mu$m diameter wires, and implies an average wire diameter of 105.2 $\mu$m. This is certainly within reason, but because of some small (∼1%) but poorly understood features in the lower channels of the Ti-K spectrum which seem to indicate a problem with the electrical connections to fpc_hb, we recommend using the theoretical model, which predicts an open area fraction of 90.26% for both fpc_hn and fpc_x2. The official open areas of the fpc_hn and fpc_x2 blocking plate apertures are therefore 3224.2 mm$^2$ and 959.2 mm$^2$, respectively, with somewhat subjective but conservatively

estimated uncertainties of 0.5%. Note, however, that the uncertainty in the *ratio* of the areas of the fpc_x2 and fpc_hn apertures is smaller (less than 0.1%), assuming that the average wire diameter (whatever it is) does not vary from one FPC to another by more than 1%.

The significance of x-rays reflecting off the window support wires and onto the window surface was also studied. Using reflectivity tables for gold, which coats the tungsten wires, a simple raytrace model showed that less than 0.01% of Ti-K x-rays hitting a wire will reflect from it, 0.08% for Al-K, 0.54% for C-K, and approximately 4% for Be-K. Since the wires block about 10% of the total window area, the net effect on the collecting area is less than 0.01% at energies above Al-K, 0.06% at C-K, and about 0.4% at Be-K. Since this effect is negligible except at extremely low energies where other terms dominate the uncertainty in QE, we have not applied any corrections for this effect.

#### Size of 36-mm fpc_hn Aperture

The BND-H mapper FPC, fpc_hn, has a 36-mm circular aperture that can be flipped in front of the full rectangular aperture. Because of the difficulty of aligning the mapper and its "flapper" aperture in situ, (particularly when the FPC was removed and reinstalled so many times, e.g., to use its aperture motor on the TMA shutter assembly), HXDS engineers noted that part of the circular aperture might fall outside the rectangular aperture, thus leading to a smaller than expected collecting area.

This hypothesis was tested during phase I and J flat field testing by exposing fpc_hn at many energies at the same location in the beam, and comparing the detected x-ray rate using the rectangular and circular apertures. The data were analyzed in two ways: assuming that the EIPS intensity was constant at each energy and, for comparison, using fpc_5 and ssd_5 for normalization. In order to minimize the effects of differences in effective window and gas transmission when using the two apertures, the average was computed using results from only those energies at which the FPC QE is greater than 75%. Results are plotted in Figure 3.1, and indicate a net open area ratio of 0.2835 ± 0.0003, which is 0.5% less than the nominal value of 0.2850. The net open area for the fpc_hn 36-mm aperture is thus 959 ± 5 mm$^2$.

## 3.3 Spectral Response Function

When fitting spectra with XSPEC, or any spectral fitting program, it is necessary to know what the output spectrum looks like when the detector is given a monochromatic input, that is, know the spectral response function, or SRF. Detailed results of FPC SRF calibration are presented in Chapter 9, but the main features are a main peak and a low-energy shelf. At energies above the Ar-K edge (at 3206 eV) there is also an escape peak that lies 2957 eV below the main peak. Background is generally a minor issue since its spectrum varies only slightly with energy and is quite stable and repeatable, although at very low energies and counting rates electrical noise may interfere with the x-ray peak. This noise is, however, essentially independent of the FPC voltage setting, and can be subtracted or modeled with little problem.

Spectral response functions were measured on fpc_x2 and fpc_hn between 70 and 1700 eV using the BESSY SX700 monochromator, which also provided QE calibration. Over 70 energies were sampled, with fine-step scans across the Ar-L, C-K, N-K, O-K, and Al-K absorption edges. Example spectra are shown in Figure 3.2. A noticeable trend is the increasing importance of the low-energy shelf as the x-ray energy is lowered. The SRF data were also used to obtain absolute QEs, since PTB has previously calibrated the SX700 beamline intensity. (FPC voltages were, of course, set to obtain the same gain vs. energy conditions as were used during AXAF calibration.)





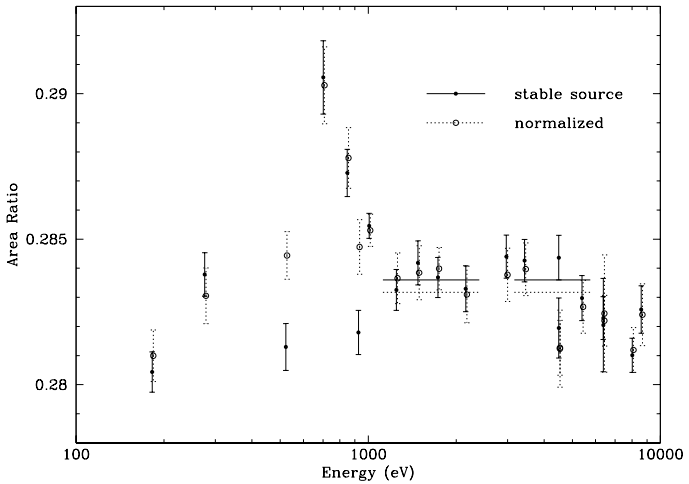


Figure 3.1: Area of fpc_hn 36-mm aperture, relative to rectangular aperture. Ratios were calculated assuming a stable source, and by normalizing to other detectors; points are slightly separated in energy for clarity. Using results from energies where QE > 75% (indicated by horizontal lines), the unnormalized average is 0.28360 ± 0.00027 and the normalized average is 0.28317 ± 0.00032. We take 0.2835 ± 0.0003 as the final answer, as listed in Table 3.3.

At higher energies, up to 5.9 keV, we used the double crystal KMC monochromator. The KMC beamline does not have absolute intensity calibration, and because of beam intensity instabilities arising from heat loading on the crystals and beamline apertures, it is difficult to obtain even relative QE information. By letting the beam stabilize and then making measurements over a relatively short period of time, however, we were able to quantify the P10 gas opacity by scanning across the Ar-K absorption edge at 3206 eV. Spectra from this scan are shown in Figure 3.3. Three features are readily observed in this series: the jump in the number of counts and the appearance of the escape peak as the x-ray energy is raised above the absorption edge threshold (thus providing precise energy calibration for the monochromator), and the nonlinearity of peak position versus x-ray energy.

This nonlinearity is caused by a discontinuity in the work function (average energy required to create a secondary electron) of the P10 gas at the Ar-K edge, as discussed in Jahoda and McCammon (1988). A similar discontinuity also occurs at the Ar-L edge, at 248 eV (see Figure 3.4); a sudden change in the fractional charge loss to the window may also be involved, since the average photon absorption depth jumps from about 2 mm to 0.2 mm as the photon energy crosses the edge. Plots of work function versus energy, normalized to 28 eV per secondary electron below the edges (the nominal value used in the `JMKmod` fitting program) are shown in Figure 3.5 (Ar-K) and Figure 3.6 (Ar-L). Although it is possible to modify `JMKmod` to include the energy dependence of the work function and/or charge loss, we have not done so since this phenomenon is only significant when trying to fit spectra in which continuum emission within the region of interest is significant so that details of energy/channel redistribution are important. Such a case may occur when analyzing white

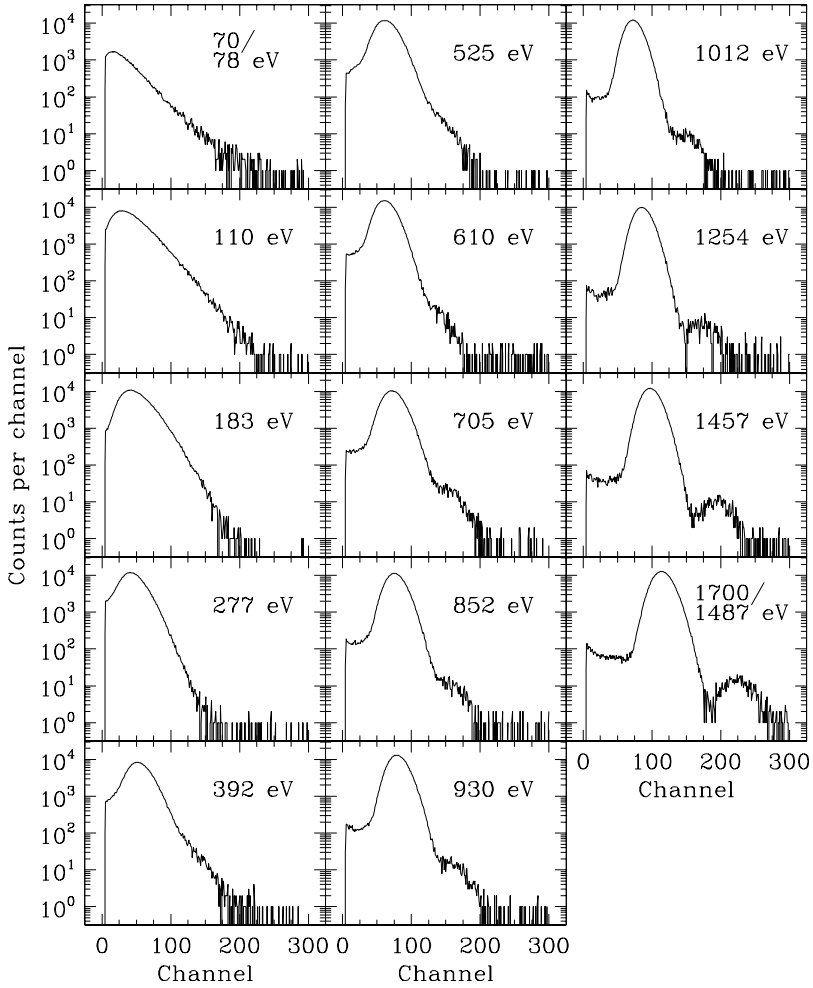


Figure 3.2: Sample spectra from the BESSY SX700 monochromator. Counting rates are generally around 4000 Hz, except for the 70-eV spectrum. Note the increasing contribution of the low-channel shelf at lower x-ray energies (see Chapter 9 for details). At higher energies, pileup and any second order diffraction are easily distinguished from the main peak.





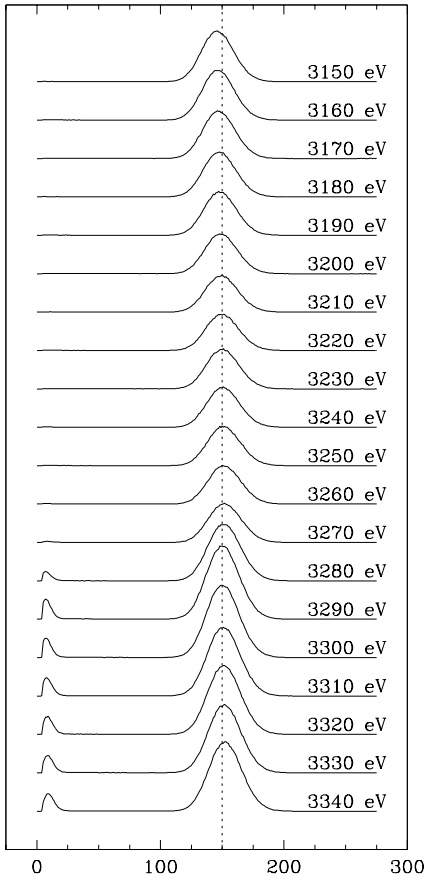


Figure 3.3: Ar-K edge scan with BESSY KMC monochromator. These data were used to measure the FPC gas opacity just below the edge. Listed energies are those requested; the true edge energy (indicated by the appearance of an escape peak and a jump in the strength of the main peak) is 3206 eV, thus calibrating the monochromator energy scale as approximately 75 eV too high. The dotted vertical line is merely to help discern relative peak positions.

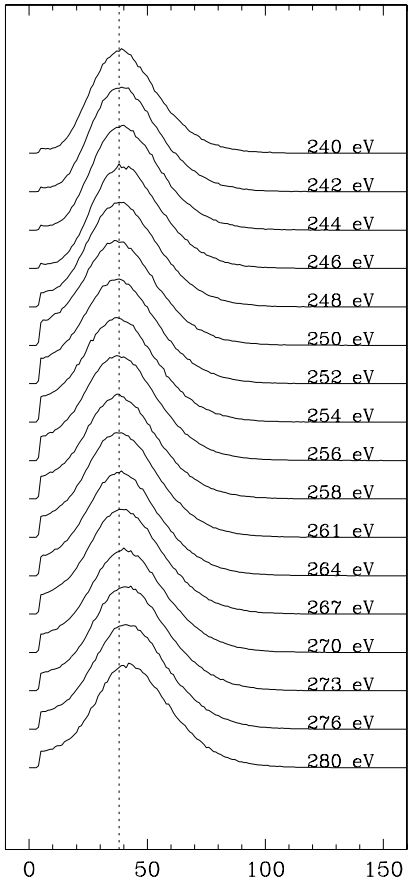


Figure 3.4: Ar-L edge scan with BESSY SX700 monochromator. Nominal $L_{III}$ edge energy is 248.4 eV. Note that the main peak position does a little "backstep" as the beam energy crosses the edges (see the vertical dotted line for reference). This change in the average energy per effective secondary electron is plotted in Figure 3.6, and Figure 3.5 for the Ar-K edge. Charge diffusion losses may also be involved, particularly at the Ar-L edge.

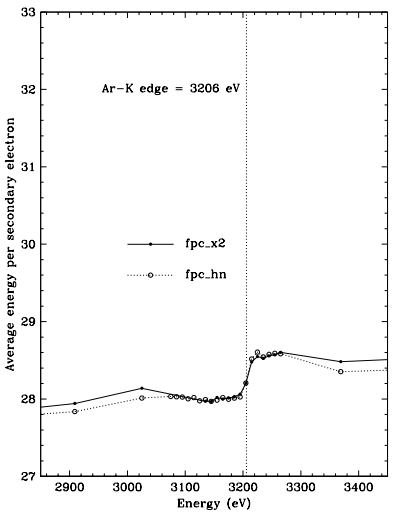


Figure 3.5: Ar-K edge work function, normalized to 28 eV below the edge. A 75-eV correction has been applied to the x-ray energies.

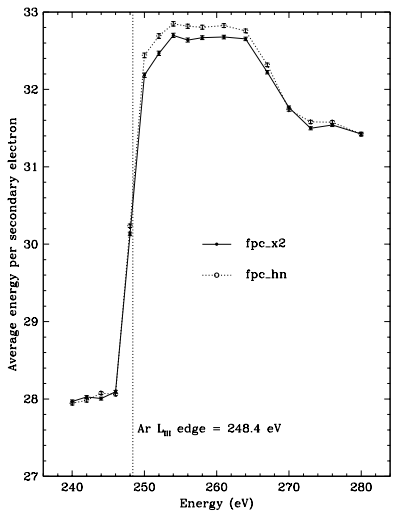


Figure 3.6: Ar-L edge work function, normalized to 28 eV below the edge. Part of the jump may arise from charge losses to the window.

beam spectra (see §3.5.2), when separating the main peak, pileup, and second order diffraction at energies between 124 and 248 eV, or perhaps when fitting C-K EIPS spectra (in which the above-edge and below-edge continua have different energy scales).

In addition to the Ar-K edge scan, about a dozen energies were sampled on the KMC beam, and measurements were often made over a wide range of energies at the same FPC voltage setting to characterize the energy linearity of the detector (although uncertainties in the energy scale of the monochromator have not yet been resolved). At energies above the Ar-K edge, spectra were often collected at several locations on the FPC—around the center, and near the short-side and long-side edges—to see how the fraction of counts in the escape peak varied. From preliminary analysis, the escape fraction appears to be fairly independent of energy (at about 8%) but slightly higher near the walls of the FPC (e.g., 8.1% vs. 7.7% in the center), as one would expect since it is more likely that an Ar-K$\alpha$ fluorescence photon will escape when it is created near a wall. Characterization of the escape fraction as a function of energy allows one to calculate the contribution of continuum-escape events to the main peak. Although the relative contributions of these events to the focal plane FPC and the BND FPCs will be different (because of the HRMA reflectivity), the net contribution to the line flux is typically only of order 1% (assuming 8% escape from a slice of continuum which has roughly 1/10 the intensity of the main line that lies 3 keV below it). Future versions of `JMKmod` (or post-fit analysis routines) will include this correction.

At energies where the P10 gas is rather transparent, spectra were also collected with the x-ray beam directly above and a few mm to one side of the anode wire. As expected, the rate of events in the main spectrum peak was lower when x-rays hit the anode wire, since no charge amplification





occurred for those events. Such spectra showed a substantial increase in the relative intensity of the shelf below the main peak, and sometimes a weak peak appeared in the low channels, presumably from photons absorbed very close to the wire that did not undergo full electron-avalanche amplification. The small effects of anode wire absorption during AXAF calibration (always less than 1%) are discussed further in §3.5.4.

Typical FPC counting rates on both beamlines were around 4000 Hz, but at several energies, spectra were collected over a wide range of rates (from less than 1000 to more than 25000 Hz) in order to study the rate dependence of the SRF, collect counting rate linearity data, or separate the effects of pileup and higher order diffraction. Sample spectra at multiple rates are shown in Figure 3.7. These data have not yet been studied in detail, but preliminary analysis has reveal no surprises. As expected, peaks become slightly broader at high rates, but the XSPEC width parameter, which must always be allowed to float, simply adjusts to give an appropriate fit.

As mentioned in Chapter 9, small changes in channel offset or amplifier gain for each detector system have no significant effect on the quality of FPC spectral fitting results, but for completeness we note that on 97/02/25 (during phase F) the fpc_hb MCB was changed from serial number 205 to 204 (the former fpc_x2 MCB) because the ADC zero level would pop up to 1.8 volts during collects. This change was made just before runid 112370.

## 3.4 Gain Nonuniformity and Anode Aging

SRF measurements made at BESSY used a narrow x-ray beam; if gas gain varies across the detector, as it does with the HXDS FPCs, then the net spectrum collected from an FPC which is illuminated over a large area will be a composite SRF. Early tests of the FPCs at SAO showed that gain varies along the long axis of the detector, being fairly flat throughout the middle and rising toward the ends because of electric field end effects; there is no gain variation in the perpendicular direction. Tests with five FPCs showed that the gain curve was virtually identical for all of them, and independent of x-ray energy and FPC voltage (see Figure 3.8).

The impact of this position-dependent gain was reduced by shortening the length of the rectangular BND-H apertures from 5" to 4", to block the regions of highest gain. The remaining nonuniformity is well characterized in `JMKmod` fits by using a delta function plus "top hat" gain distribution curve for the BND-H FPCs, with fit parameters $gain_2 = 1.05 \times gain_1, dgain_2 = 0.1 \times dgain_1$, and $norm_2 = 0.724 \times norm_1$, as described in Chapter 9. (The top hat is not necessary for the focal plane or BND-500 FPCs, or when fpc_hn is used with its circular aperture.) Just to be sure that shortening the blocking plate apertures had no unexpected effects, the gain curve for fpc_hn was checked again at BESSY following AXAF calibration, and found to be unchanged, except that the high-gain ends were indeed excluded.

Another gain phenomenon is anode aging, in which nonconductive polymeric compounds formed during the electron avalanche process are deposited on areas of the FPC anode wire which collect the charge. The rate-dependent effect of such deposits is to reduce the gas gain and degrade energy resolution. Generally speaking, the amount of gunk deposited on the anode is proportional to the cumulative charge per unit area collected on the wire, and the rate of deposition can be reduced by using extremely high-purity gas and scrupulously clean hardware free of silicon and halogen compounds (Kadyk, 1991). Following these prescriptions, great care was taken when assembling the two gas supply systems, in Building 500 and the Instrument Chamber, and unnecessary exposure to x-rays was avoided during AXAF calibration.

The FPC most likely to suffer from anode aging was fpc_x2 because it collected the largest x-ray dose over the smallest area. During AXAF calibration, one aging diagnosis test was successfully

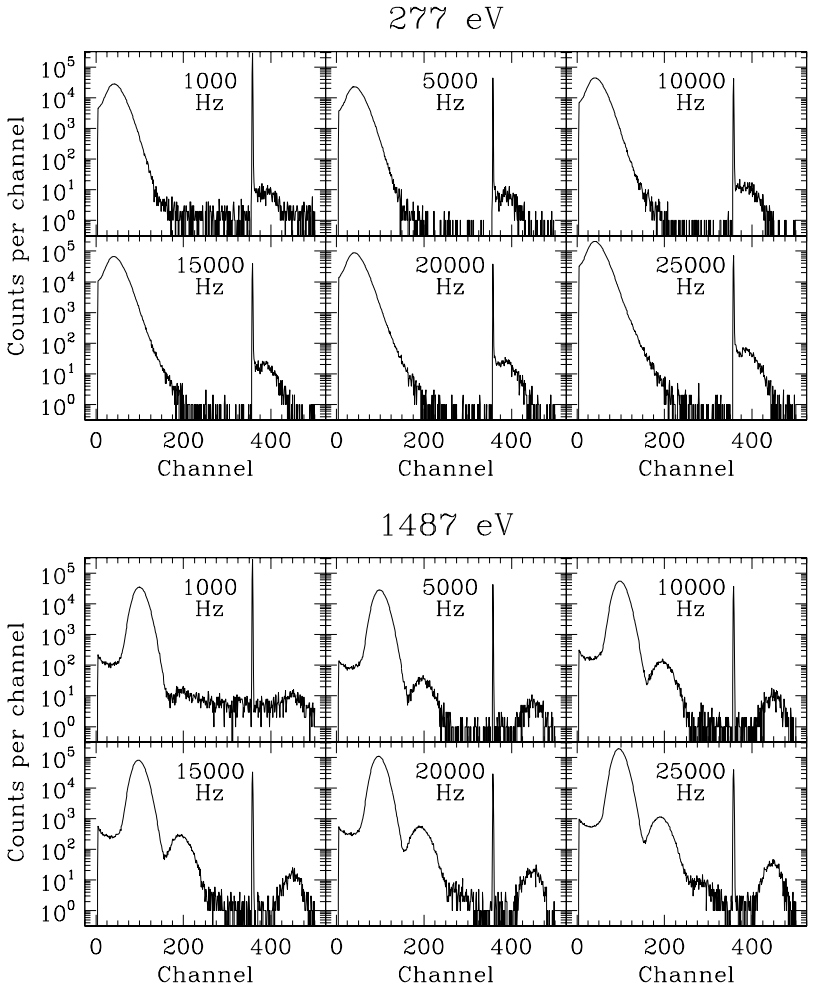


Figure 3.7: Sample spectra over a wide range of counting rate. These data can be used to measure the accuracy of deadtime-correction methods by comparing the detector counting rate with the synchrotron ring current, to study how the spectral response function varies as a function of rate, and to separate the effects of pileup and monochromator higher order contamination (since pileup is rate dependent but the fraction of higher order diffraction is not).





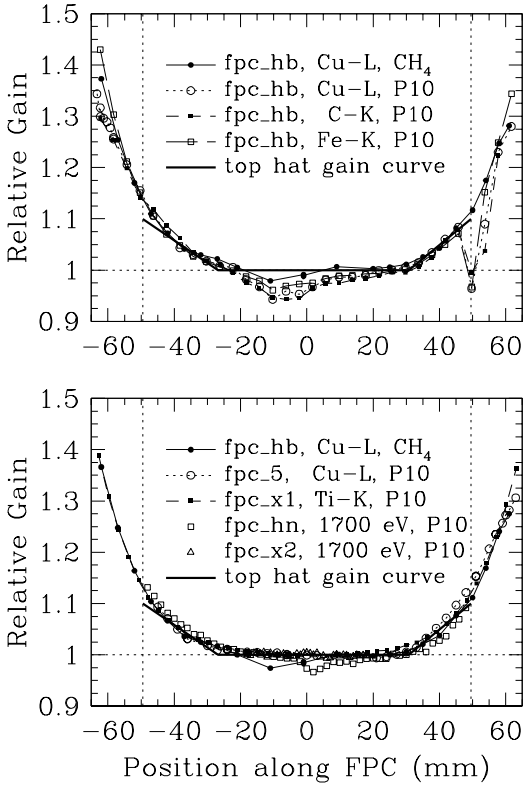


Figure 3.8: Gain scans for (top) a single FPC at several energies and with two kinds of gas, and (bottom) for several different FPCs. Vertical dotted lines mark the edges of the 99-mm blocking plates. In the top plot, the sharp dips in the P10 curves near one end are the result of an anode aging test conducted after the methane gain scan. The slight dips near the center are also from anode aging.
In the bottom plot, the curves for the five FPCs are nearly identical, and their characteristic shape (flat middle plus linearly rising ends) is well represented by the recommended `JMKmod` delta function plus "top hat" gain distribution model with $gain_2 = 1.05 \times gain_1, dgain_2 = 0.1 \times dgain_1$, and $norm_2 = 0.724 \times norm_1$. The fpc_hn curve has a slightly different shape, but the averaged-about-the-center gain curve is the same as for the other FPCs to better than 1%. The curve for fpc_x2, from -18 to +18 mm, is featureless and flat. The slight amount of anode aging seen in fpc_hn and fpc_hb only shows up because they were exposed to small, high-intensity beams; in normal flat-field operation the amount of gain depression, which roughly scales with x-ray intensity per unit length, is completely negligible.

completed (TRW-ID D-IXF-FA-4.013), which showed no detectable degradation in performance. A more thorough check was conducted at BESSY in December 1997, scanning in 1-mm steps along the anode wire to look for gain variations or degraded energy resolution, which confirmed that the gain curve was still perfectly flat. (The BESSY scans of fpc_x2 and fpc_hn are included in Figure 3.8). Surprisingly, a scan of fpc_hn did show a little gain depression near the center, presumably from early testing at SAO using methane, but that only appeared because of the small, high-intensity beam used to do the scan. In normal operation at the XRCF, the degree of gain depression, which roughly scales with x-ray intensity per unit length (see Algieri et al. (1994)), is completely negligible because incident x-rays are spread out over the entire BND aperture.

## 3.5 Quantum Efficiency

Probably the most important FPC characteristic to calibrate, and the most difficult and complex, is quantum efficiency. A large body of QE calibration data has been collected, both in flat field experiments at XRCF, and in the synchrotron at BESSY. The QE estimates provided here are much better than those provided previously, but may be refined at the percent level in the coming months.

A plot of FPC QE, approximated as the product of window transmission and gas opacity, is shown in Figure 3.9, along with a simple model of SSD QE for comparison. The true quantum efficiency of each FPC, which is defined to include the low-energy shelf and any escape peak, was determined in a variety of ways, depending primarily upon the x-ray energy. In general, absolute QEs for fpc_hn and fpc_x2 are derived using the BESSY SX700 monochromator between 80 and 1700 eV, with the primary sources of error being the calibration of the efficiency of the monochromator and the photodiode used to monitor the storage ring current. Net uncertainty is typically 1-2%, and somewhat worse below 200 eV; see Auerhammer et al. (1998) for details. The transmission of the fpc_x2 window was also measured on the SX700, and gas opacity at 1700 eV at several gas pressures was studied (unsuccessfully). The KMC beamline is not calibrated, but we did obtain some QE information by scanning across the Ar-K edge at 3206 eV.

Above 1700 eV, apart from the BESSY Ar-K edge data, we rely on calibration relative to the SSDs, using the flat field measurements at XRCF in November 1996 and during Phases I and J to provide the relative QE of all FPCs and SSDs (although errors accumulate relatively rapidly given the chain of beam maps and QE comparisons that are required to relate the BND-500 SSD to the BND-H and HXDA FPCs). The SSDs were themselves absolutely calibrated at high energies at BESSY using the white light beam and calibrated filters, and since their QE is nearly 100% above 1700 eV, the uncertainty in their QEs should be relatively small. (Note, however, that as of this writing the analysis of SSD calibration data is incomplete.) White light calibrations were also conducted for fpc_hn and fpc_x2, but the combination of broadband radiation, poor energy resolution, energy scale nonlinearities, and other factors greatly complicates analysis, so results are considered to be significantly less reliable than those obtained from comparisons with the SSDs. It should be possible, however, to extract reliable measurements of gas opacity (see §3.5.1) just below the Ar-K edge at 3206 eV from the Fe- and Cr-filtered spectra. Preliminary results from the white beam calibration and other BESSY measurements have been published by our PTB collaborators in Auerhammer et al. (1998).

As will be explained in more detail in §3.5.1:"Window Bowing and Nonuniformity" and §3.5.4, "Relating Flat Field, HRMA, and BESSY measurements", in order to apply QE calibration results to analysis of AXAF calibration data, one must take into account in how an FPC was used as it was being calibrated and how it was used for calibrating AXAF, since differences in gas temperature





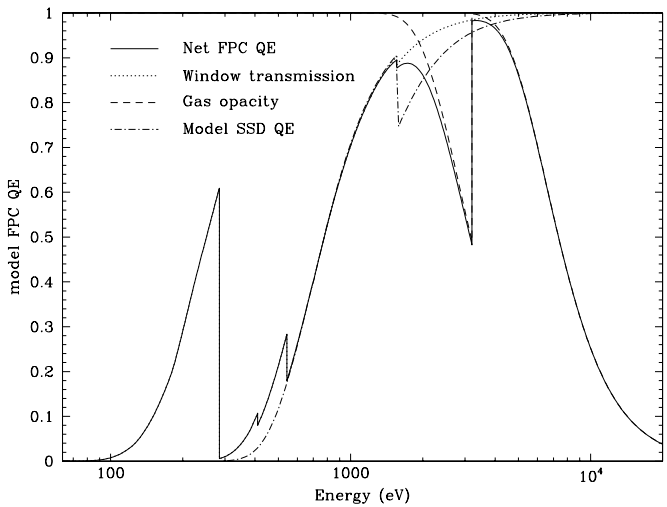


Figure 3.9: Model FPC QE. Net QE is the product of window transmission and gas opacity, assuming: 1.0 $\mu$m polyimide ($C_{22}H_{10}O_4N_2$) with a density of 1.3 g/cm$^3$, plus 200 Å of Al with a density of 2.6941 g/cm$^3$; 90.01% Ar plus 9.99% $CH_4$ at 400 torr and 10 °C, with an average gas depth of 55.93 mm. SSD QE was modelled as the transmission of 1.25 $\mu$m parylene ($C_8H_8$, density 1.10 g/cm$^3$) plus 2000 Å of Al. The 1995 Henke tables were used.

and the size and angle of incidence of the x-ray beam can lead to differences in effective QE of up to several percent, although the typical variation is much less. Table 3.4 summarizes the differences among the various test situations; keep them in mind while reading the rest of this section on Quantum Efficiency.

### 3.5.1 Monochromator Results

#### Absolute QEs from SX700

Between 80 and 1700 eV, the BESSY SX700 monochromator provides a well calibrated beam intensity with a beam size of approximately 600 by 300 $\mu$m FWHM, which neatly fits within the "sweet spot" of the central 2mm by 2mm windowlet. By monitoring the BESSY ring current, applying the monochromator efficiency calibration, and making deadtime and pileup corrections to the FPC spectra, the QEs of fpc_hn and fpc_x2 were measured from 80 to 1700 eV at over 70 energies, with fine-step scans across the Ar-L and C-, N-, O-, and Al-K edges. At the lower energies, the contributions of higher-order diffraction peaks and pileup (which are generally no more than a few percent) were removed by fitting a second peak fixed at twice the energy of the main peak. Net uncertainties are usually of order 1%, although worse at very low energies. As previously noted, these data were also analyzed to characterize the FPC spectral response functions, using the `JMKmod` fitting procedure with a single delta-function line, as described in §9.5.

We present in Figure 3.10 plots of the absolute quantum efficiency of the fpc_hn and fpc_x2 detectors over the range from 0.08 to 1.7 keV, when exposed to small beams in their central

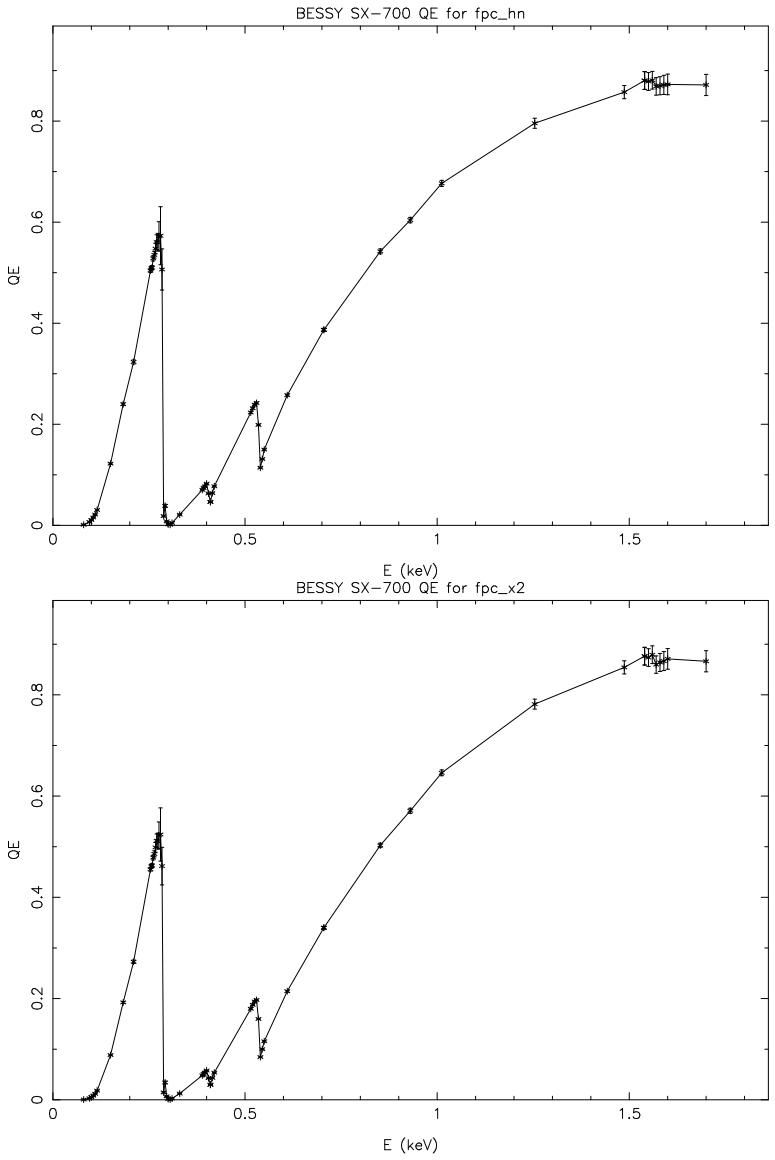


Figure 3.10: Absolute quantum efficiency for fpc_hn (top) and fpc_x2 from JMKmod fits to BESSY SX700 monochromator data





| Test format | X-ray angle | Beam size | Approx. gas temp. |
|---|---|---|---|
| BESSY | normal incidence | smaller than windowlet | 30°C (fpc_x2, fpc_hn) |
| Flat Field | normal incidence | blocking plate apertures for BND-H and fpc_x2, regular 4, 12, 36-mm aps for fpc_5 | 20°C for BNDs<br>30°C for fpc_x2 |
| HRMA | normal for BNDs, up to $\sim 4°$ for fpc_x2 | focussed beam, concentrated in rings on central windowlet; for off-axis or grating measurements, image may extend across more than one windowlet. | 10°C for BND-H<br>20°C for fpc_5, fpc_x2 |

Table 3.4: Differences among test environments.

windowlets. Note that the error bars are relatively large near the C K edge (0.284 keV), due to SX700 facility effects (*e.g.* carbon contamination). Although two sets of measurements were made at 0.705 keV, only the results from one are shown; the second set is 4.5% higher for each FPC. Perhaps, although we hope and believe not, this indicates the irreducible error level of these measurements.

As another accuracy assessment, we divided the QE of fpc_x2 by that of fpc_hn to form a relative QE (RQE) for fpc_x2, as we did for the XRCF flat field experiments described later in §3.5.3. We plot in Figure 3.11 both of these curves, and the ratio of these two determinations. Although no adjustments have been made for window transmission nonuniformities (which will affect comparisons of BESSY vs. XRCF flat-field QEs at the ∼1% level), agreement is generally quite good, although it appears that there may be a systematic discrepancy in results derived from the two test locations.

### Window Transmission

In addition to measuring the QE of assembled FPCs, we also measured the transmission of the central windowlets of the windows from fpc_x2 and fpc_5, along with a sample of unstretched (i.e., never mounted on an FPC or pressurized to 400 torr) window material. These in/out measurements were made at approximately 380 energies between 40 and 1700 eV, with 1-eV steps across absorption edges, using a calibrated photodiode. As one would expect, the transmission of the unstretched window was lower than that for either of the stretched windows, since the act of pressurizing windows permanently deforms them, although there is, of course, some relaxation between the pressurized and unpressurized states. Transmission curves are shown in Figure 3.12. The nominal uncertainty of these measurements is typically 2% (PTB has provided more detailed estimates of uncertainties as a function of energy), but at energies where transmission is substantially less than 10% the uncertainty may be quite a bit larger—see, for example, the wiggles around 110 and 350 eV.

One would expect that since window transmission is given by $\exp(-\mu\rho t)$, the ratio of the logarithms of two windows' transmissions should be equal to the ratio of their thicknesses (assuming that the composition and density of the two windows are the same), and indeed, we find that an energy-independent ratio of $t_{x2}/t_{unstretched} = 0.93$ fits the data very well. Similarly, if the net FPC QE is simply the product of window transmission and gas opacity, then window transmission and net QE should be the same below ∼1700 eV, since gas opacity is nearly 100%.

In Figure 3.13 we plot such a comparison for fpc_x2, and find that the QE is systematically lower than the window transmission. In the lower figure, we plot the shelf norm *vs.* the ratio of the

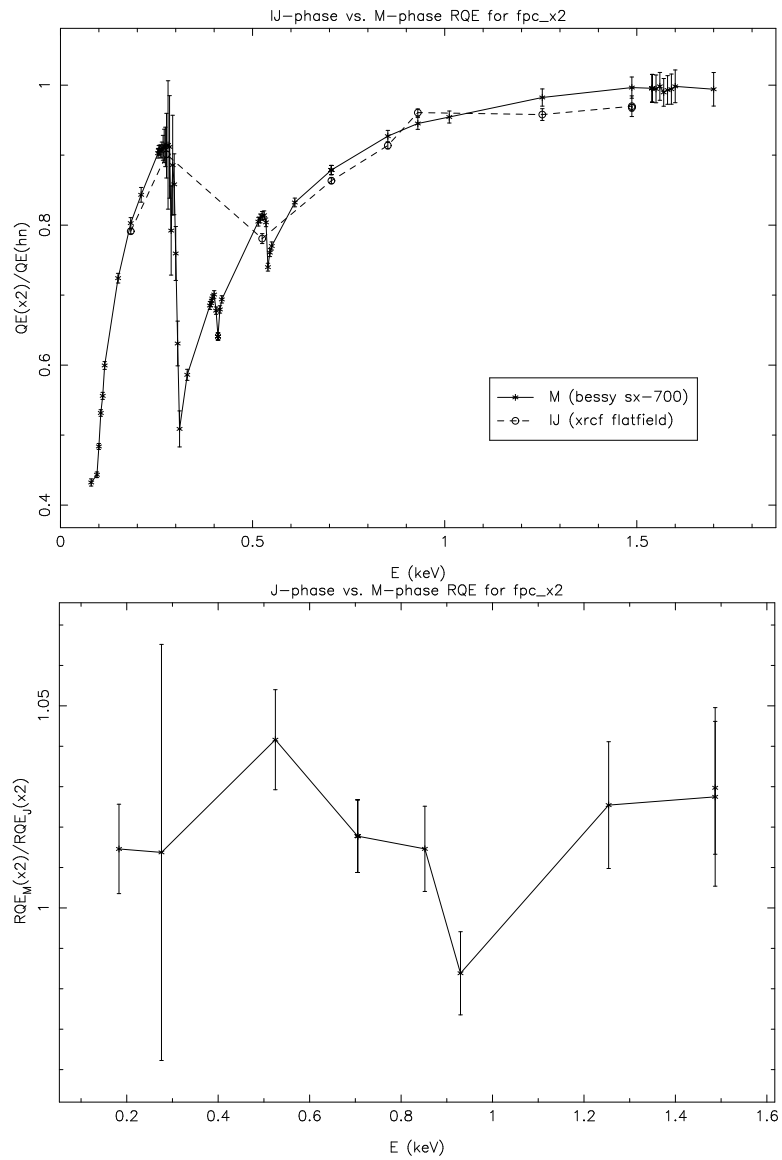


Figure 3.11: Relative quantum efficiency for fpc_x2 from BESSY (phase M) and XRCF (phases I & J) flat field measurements (top) and ratio (bottom)





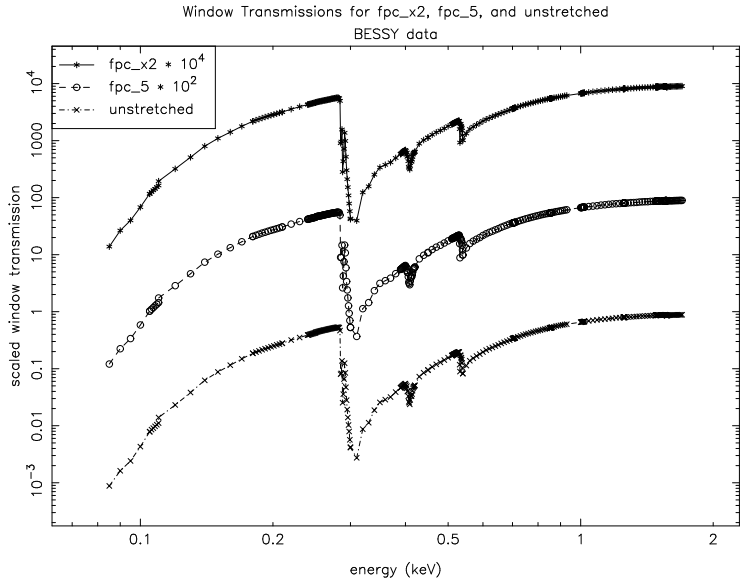


Figure 3.12: Transmission of 3 FPC windows as measured at BESSY. The windows are those of the fpc_x2, fpc_5, and an unstretched window. The first two curves are scaled for clarity.

detector QE to the window transmission. Except for spikes which may arise from fitting effects near the nitrogen and oxygen edges, the two quantities trend together. This suggests that the QE deficit may be an effect of charge loss to the window, which is also measured by the shelf normalization; we are consulting with outside experts regarding this idea.

Another possibility is that the window measurement was made in a different, lower-transmission windowlet than for the assembled-detector QE measurement; the windows barely fit inside the reflectometer chamber used for the measurements, and there were only a few mm of travel for alignment. Analysis of fpc_x2 window uniformity data will shed light on this matter.

### Window Bowing and Uniformity Mapping

When applying any BESSY calibration data it is important to remember that analysis of HRMA calibration data requires that we know the QE of fpc_hn when exposed over its entire window, not just the center of the central windowlet, as with the BESSY measurements. We therefore measured the relative QE of fpc_hn (and fpc_x2) at the center of many windowlets in order to characterize large-scale window uniformity (see Figure 3.14). Strictly speaking, such a comparison is not necessary for fpc_x2 since we are ultimately interested in knowing its QE when exposed to x-rays focussed on the central windowlet, i.e., as used for HMRA calibration. Relating fpc_x2 QEs in BESSY and flat field tests, however, does provide a check on results for other FPCs that are derived from flat field comparisons with fpc_hn.

When applying BESSY calibration results to XRCF measurements, it is also necessary to con-

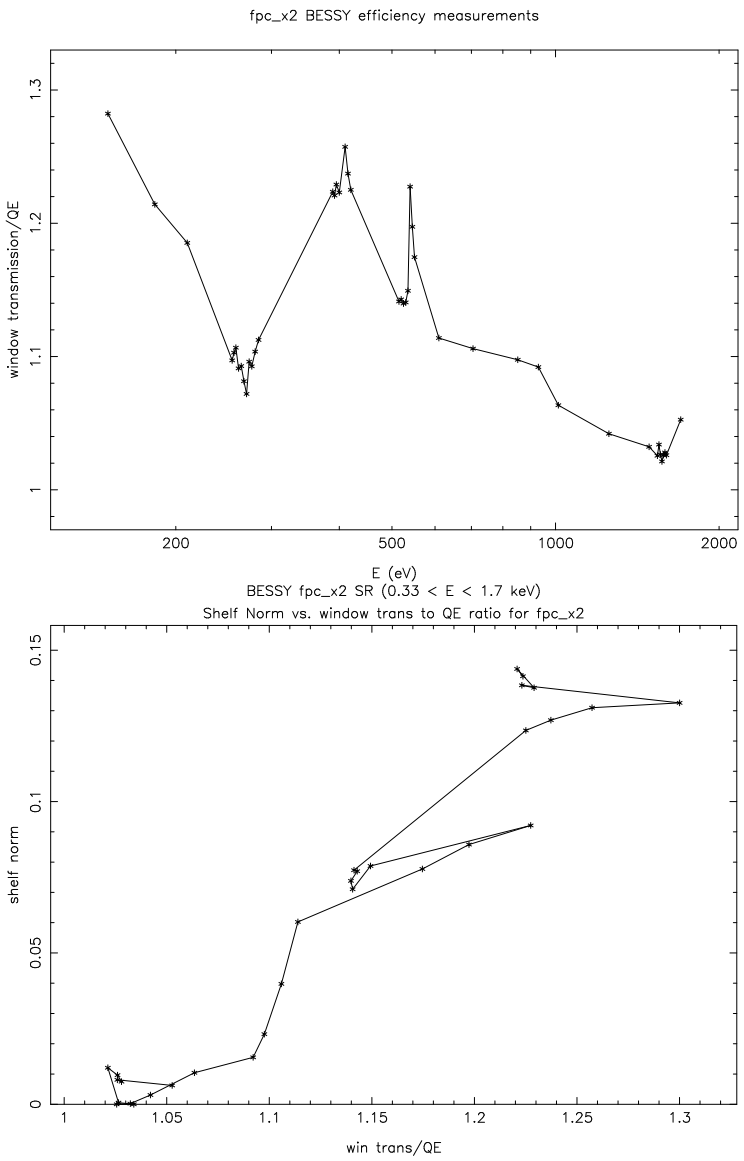


Figure 3.13: Ratio of fpc_x2 window transmission to QE *vs.* energy (top) and *vs.* shelf norm (bottom). This suggests the QE deficit may be due to charge loss to the window.





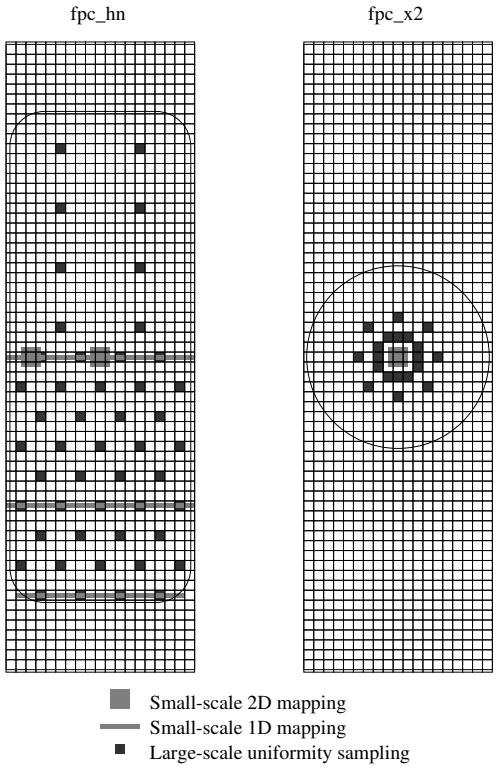


Figure 3.14: QE mapping of fpc_hn and fpc_x2. Drawings show full window assembly (1.5" by 5.0" with 2-mm wire spacing), with blocking plate apertures for fpc_hn and fpc_x2. Small-scale scans used five points per windowlet, in 350-$\mu$m steps. Most QE mapping was conducted at 330 eV; some scans were repeated at 500 and 930 eV. Mapping pattern for the two-dimensional small-scale scans is shown in Figure 3.16. SRF/absolute QE measurements were made in the center windowlets (or 2 mm to the side when using the higher-energy KMC beam, so that penetrating x-rays would not hit the anode wire running down the middle).

sider the effects of window bowing. In addition to a global deflection of the support wires of about 1.25 mm, the center of each 2-mm by 2-mm windowlet extends about 0.25 mm beyond its surrounding support wires (Goddard (1994)—see Figure 3.15), and the window surface is angled at approximately 15 °next to the wires (Cohen (1995)). The net QE of fpc_hn will therefore be lower at the XRCF than at BESSY because the average path length through the window for normally incident x-rays is longer. The effective thickness also depends on the angle of x-ray incidence, which can be several degrees from perpendicular for fpc_x2 at the XRCF. There are also true thickness variations in the polyimide caused by stretching between the wires.

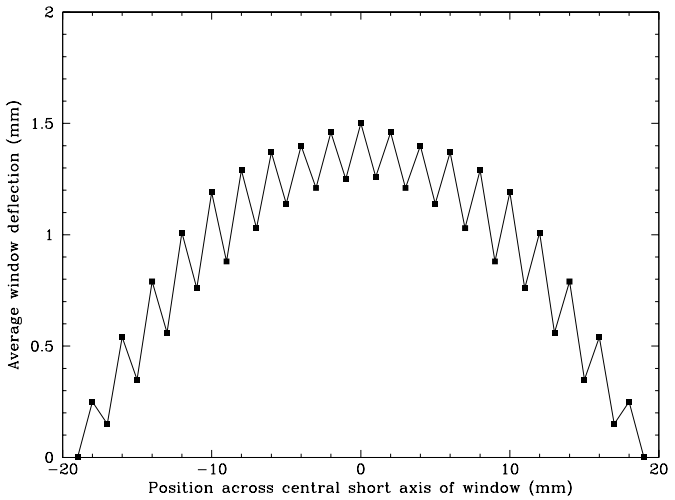


Figure 3.15: Measured deflection of the polyimide/Al window material across the central short axis. The average is shown from three windows, all measured at the standard operating pressure of 400 torr. Deflections were measured in the center of each windowlet and underneath the support wires. Variation between the two most different windows was typically 0.30 mm.

At low energies where window transmission is small, these differences in effective thickness can produce relatively large differences in QE. As an example, at O-K (525 eV) window transmission is approximately 0.250 at normal incidence, but only $(0.250)^{\sec 15^\circ} = 0.238$ at 15 °(near a support wire), a relative difference of 5%. At 95 eV, where window transmission is roughly 0.0040, the relative change is nearly 20%. Determining the effective QE of an FPC, particularly for grating measurements of intrinsically broad lines (which have the added complication of spanning a range of energies with a corresponding range of window transmissions), can therefore be a complicated enterprise.

To characterize the effects of bowing within a windowlet, we conducted fine-scale scans with the smallest possible beam (600 × 250 $\mu$m FWZI, as determined from beam profile scans across the edges of the fpc_x2 blocking plate aperture) around the central windowlets of fpc_hn and fpc_x2, and along three lines across the short axis of fpc_hn. The layout of these mapping measurements is shown in Figure 3.14 and Figure 3.16.





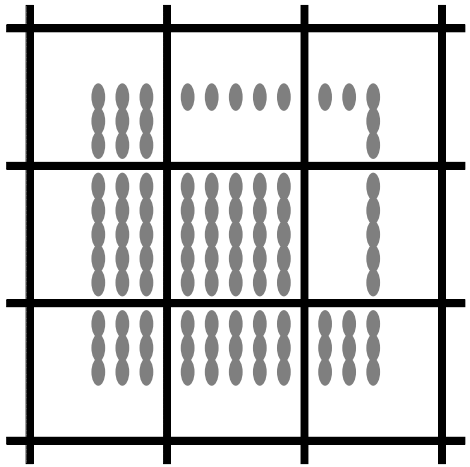

Figure 3.16: Small-scale 2D QE mapping. Data from these scans (conducted at the three window locations shown in Figure 3.14) will be used to characterize windowlet bowing and how it changes the effective QE of an FPC depending on the x-ray illumination pattern. Dark lines are the 100-$\mu$m-diameter support wires, 2 mm apart. The x-ray beam was approximately 600 $\mu$m × 250 $\mu$m full width at zero intensity, and FWHM was less than 300 $\mu$m × 200 $\mu$m. The beam size shown is 400 $\mu$m × 200 $\mu$m, with the short axis of the window lying horizontally.

Most of the large- and small-scale scans were conducted at 330 eV, but a few were made at 500 and 930 eV as double-checks. 330 eV was chosen because window transmission is very low there (about 2% for fpc_hn and 1% for fpc_x2), and so differences in window thickness will lead to relatively large differences in transmission, but the energy is still high enough to produce a well defined peak in the spectrum. An energy just above the C-K edge (at 284 eV) would have been better from that standpoint, but scattering from carbon contamination on the monochromator optics would introduce an unresolvable 277-eV component into the spectra.

Although these data have not yet been analyzed, plots of ROI-summed rates versus position are shown for the central short-axis scan of fpc_hn in Figure 3.17. Rates have not been corrected for beam decay, and each curve has been rescaled for plotting purposes, but it is clear that there can be significant variations in window thickness on fairly small scales; the roughly 25% peak-to-peak jump seen in the 330-eV center scan corresponds to approximately a 6% difference in window thickness. Rates for the 500-eV scan confirm that there is thickness nonuniformity, although the manifestation is much less pronounced because the window transmission at 500 eV is so much higher (20% vs 2%). The effect of bowing within each windowlet can also be seen in both sets of data.

### Gas Opacity

At 1700 eV, the high end of the SX700 monochromator's energy range, we attempted to measure the opacity of the P10 gas in fpc_hn and fpc_x2 by comparing the detector counting rates at gas pressures of 400, 300, 200, and 100 torr. From those relative rates, and by estimating the small

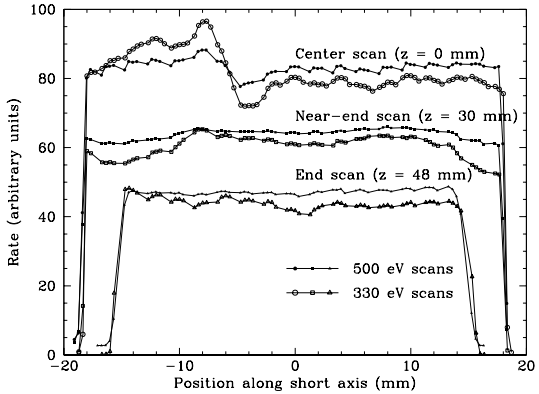


Figure 3.17: 1D QE mapping scans of fpc_hn. Rates are arbitrary and have been scaled to facilitate comparison of 330 and 500 eV results. Rates have not been corrected for beam decay, which is approximately 7% for the 330-eV data from left to right; beam decay is much less for the 500-eV scans. Note the sharp nonuniformity in the center scan and the reproducibility of results at different energies, after taking into account that variations in window transmission at 500 eV will be much smaller than at 330 eV.

opacity of the methane component (which composes 10% of the P10 partial pressure) and assuming that the Henke absorption coefficients are correct at all energies apart from a small scaling factor, the product of the gas depth and argon absorption coefficient at 1700 eV could be determined. From this, we could derive a scaling factor to use in our model of gas opacity, and then perhaps apply it at higher energies where we cannot directly obtain absolute QE calibration.

Unfortunately, the x-ray beam was centered on the central windowlet of the two FPCs, and as the gas pressure was reduced some of the x-rays penetrated the gas and hit the anode wire running down the middle of the FPC, producing a stronger shelf feature. Although this was a few-percent effect, it was enough to preclude the extraction of useful information from the measurement. (In future runs on the higher energy KMC beam, spectra were collected with the x-ray beam offset by 2 mm, so that anode wire absorption was not a problem.)

Despite the lack of beamline intensity calibration for the KMC monochromator, we were able to measure QE at a higher energy by scanning across the Ar-K absorption edge and recording the relative counting rates just below and above the edge. Because there is no intensity monitor on the KMC beamline, and intensity can vary with time because of thermal instabilities, we tried to let the beam stabilize so that relative rate comparisons would be valid. Analysis of data from the first energy scan, with fpc_hn, indicates that the beam was still unstable at the $\leq$10% level. The second scan, with fpc_x2, is believed to be valid at the one or two percent level based upon the amount of scatter in the counting rates at similar energies, but we have no way of knowing for sure. The fpc_x2 scan covered the range 3135 to 3265 eV (after applying a 75-eV energy correction) in 10-eV steps, as shown in Figure 3.18.

Taking the average of the 6 points between 3135 and 3185 eV (sample standard deviation 4.3% divided by $\sqrt{5} = \pm 1.9\%$) and the 5 points between 3225 and 3265 eV ($2.5\%/\sqrt{4} = \pm 1.2\%$), and adjusting for ring current decay (approximately 0.5% per minute) and the theoretical energy





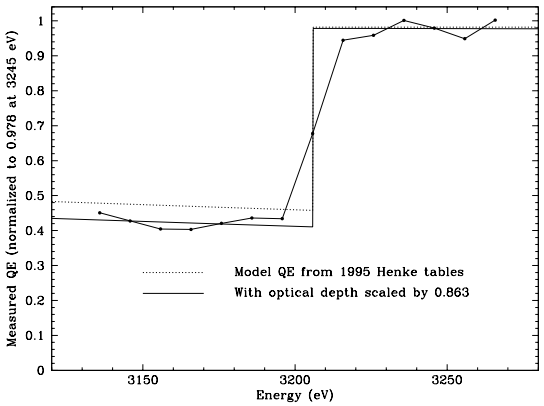


Figure 3.18: fpc_x2 QE at Ar-K edge. Relative QEs at 33.994 °C below and above the edge were derived from measured rates, after correcting for monochromator efficiency and beam decay. Assuming window transmission is 0.985, net QE at 10 °C is 0.9804 at 3245 eV and 0.4500 ± 0.0010 at 3160 eV.

dependence of the monochromator's output spectrum with silicon crystals (about a 9% difference between 3160 and 3245 eV) the QE as measured at 33.994 °C at 3160 eV is $0.4333 \pm 0.0010$ times that at 3245 eV.

If we then assume that net QE is equal to window transmission (which our model predicts is 0.985 at both energies) times gas opacity, without any other effects such as charge diffusion losses, and if we further assume that our theoretical models of window transmission and gas opacity are close to reality, apart from absorption coefficient scaling factors, we can determine the QE at both energies. We thus derive gas optical depths of 4.950 at 3245 eV and 0.5627 at 3160 eV, which are equal to $0.863 \pm 0.026$ times the values computed in our theoretical model, which assumes a net gas depth (with window deflection of 1.08 mm) of 56.10 mm, with 90.01% Ar and 9.99% methane, at 400 torr, using the 1995 Henke tables. The derived optical depth scaling factor is close to that derived from flat field normalization relative to the SSDs (see §3.5.3), but all the SSD-dervied results should be considered as somewhat preliminary at this time.

After adjusting for gas temperature, we finally obtain QEs at 10 °C of 0.9804 at 3245 eV and 0.4500 ± 0.0010 at 3160 eV. Note that the quoted uncertainty is purely statistical, and does not include systematic uncertainties in the values of KMC efficiency, beam intensity stability, or model FPC QE (such as from charge diffusion losses above the Ar-K edge). Any or all of these uncertainties, particularly the KMC efficiency, could reasonably be a few percent.

### 3.5.2 Absolute Broad Band

As with the SSDs (see Chapter 4), broadband QE was measured for fpc_hn and fpc_x2 on the BESSY white beam, which provides a pure synchrotron spectrum whose exact shape and intensity can be calculated from first principles based on precise knowledge of the ring energy, magnetic field, and the distance to and solid angle subtended by the detector aperture. In order to sample the detector QE over different energy regions, spectra were also collected with various thin filters—2.0-$\mu$m Be, 0.6-$\mu$m Fe, 1.5-$\mu$m Ti, and 2.0-$\mu$m Cr—placed into the beam (see Figure 3.19). The

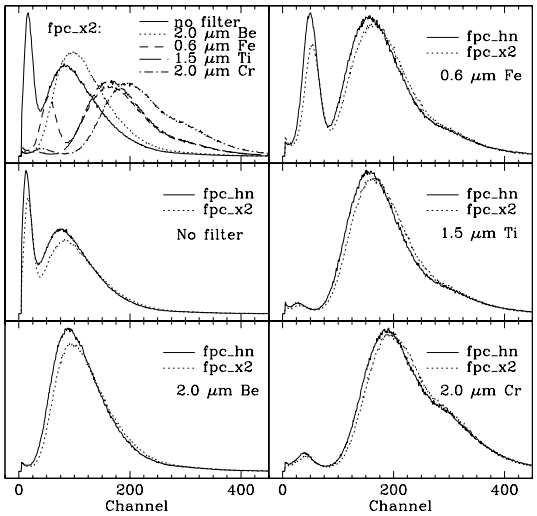


Figure 3.19: White beam spectra. Vertical scale is arbitrary, but the same for each curve within a given panel. Various filters were chosen to calibrate the absolute QE of the FPCs in different energy ranges. As already seen in the SX700 data, fpc_hn has higher QE than fpc_x2 at all energies. The difference in window thicknesses is, of course, most apparent at low energies, as seen in the spectra with the null and 0.6-$\mu$m Fe filters. Note that gains may be slightly different when comparing fpc_x2 and fpc_hn.

transmission of the Be, Fe, and Cr filters was measured at many energies up to 1900 eV during in/out tests with the PTB photodiode on the SX700 beamline, although the Be filter which was calibrated was not the same as the one used for the white beam QE measurements; the original broke after being calibrated, so a spare filter cut from the same foil was used on the white beam. Time constraints did not permit calibration of the Ti filter.

The transmission of each of these filters was measured during in/out tests with the PTB photodiode on the SX700 beamline, except that the Be filter which was calibrated was not the same as the one used for white beam testing; the original filter broke after being calibrated, so a spare filter cut from the same foil was used on the white beam. Also, time constraints did not permit calibration of the Ti filter.

A 1.5-mm aperture was fixed in front of a windowlet 2 mm off the center, so that anode absorption effects would not be present. Unfortunately, the alignment of the detector and beamline had to be adjusted while under vacuum in such a way that the entire detector chamber was slightly askew, with the result that the aperture was centered about 0.6 mm off-center from the 2-mm-square windowlet for both FPCs (as determined from x-ray scans). This makes data analysis more complicated, since the effects of wire blockage and window bowing must be considered. Because of these difficulties, the uncertainties in filter transmission calibration and the energy scale and linearity, and the general problem of interpreting a broadband spectrum with poor energy resolution, we have not yet analyzed the white beam data. A casual inspection, however, shows that the QE of fpc_hn is higher than that of fpc_x2 at all energies (as already determined from SX700 and flat





field measurements), and that the difference is more pronounced at low energies (see the Fe-filtered spectrum and compare the low and higher energy peaks). Despite the analysis problems mentioned above, it is likely that the Fe- and Cr-filtered spectra can be used to infer a fairly accurate optical depth for the P10 gas just above the Ar-K edge.

### 3.5.3 Relative QEs from Flat Field Calibration

During April and June of 1997, a series of flat field experiments were conducted at XRCF, after shipment of the HRMA to TRW. The first set, phase I, were conducted with the flight ACIS camera at the focal plane, the BND equipment in its usual places, with the exception that the fpc_x2 detector from phase 1 was put in place of the fpc_hs. The second set of tests, phase J, were conducted with all HXDS equipment in place, but with certain detectors swapped. The detector locations for the various phases are summarized in Table A.1.

During phase J, numerous experiments were done with the Electron Impact Point Source (EIPS) tuned to many of the energies used during the HRMA calibration. These runs were long enough to collect high signal-to-noise pulse-height spectra in each detector and thus allow a high precision cross-calibration of the various detectors. For most of the detectors, the combination of relative quantum efficiencies measured in phase J with absolute QEs from those few which were measured at BESSY, will be the only available absolute quantum efficiency numbers. Since there was no calibration of FPC QE above 1.7 keV at BESSY except for the indirect measurement at the Ar-K edge, the flat field data comparison between the FPC and SSD detectors at these higher energies is crucial for the understanding of this important quantity.

We present in Table 3.5 the results of these experiments.

Data for these tests were reduced as in §9.4, using double-`JMKmod` models in XSPEC. This accounts for the nonuniformity of the gain in the open fpc_h detectors. Single `JMKmod` models were used for the fpc_x2, since the smaller open area presents a nearly uniform gain to the incoming x-ray beam. Backgrounds were extracted from temporally nearby tests conducted during x-ray source system downtimes, modeled usually as a broad Gaussian plus a falling powerlaw, and then included in the fits with no free parameters. The C-statistic was used.

Using the distances listed in Table A.3, and aperture sizes listed in Table A.2, we then constructed fluxes for each detector, extrapolated to the source distance of the HRMA entrance. Beam uniformity factors were created for each iteration, (§12.4) and the position of the mapping detector with respect to the other detectors was noted. Selecting an iteration in which the mapping detector was in its home position, we then constructed relative quantum efficiencies, as discussed in §12.5.

We have then applied temperature corrections, to make the relative QE values in the table those appropriate to 10°C. This procedure is outlined in §3.5.4.

The two classes of experiments produce two different types of results. The BND-H beam uniformity maps allow us to compute the ratio of the QE of each of the fpc_h detectors and the fpc_x2 to one detector in this set, and fpc_hn was chosen to be that fiduciary detector. The Phase I tests, since the fpc_hs was not involved in the experiment, do not produce relative QE numbers for this detector.

The other type of experiment, BND-500 beam uniformity maps, allows computation of the relative QE of three detectors: the ones in the ssd_5, fpc_5 positions, and, when the gate valve was open exposing the BND-H detectors, the fpc_hb. Note that in phase J, these detectors were those otherwise known as ssd_x, fpc_x1, and fpc_hb. We have therefore computed the ratio of the QE of each of these detectors to that of the fpc_5 detector for that phase (*i.e.* fpc_5 for phase I and fpc_x1 for phase J). These data are presented in Tables 3.6 – 3.8.

| E (keV) | Line | fpc_hs/fpc_hn | | fpc_ht/fpc_hn | | fpc_hb/fpc_hn | | fpc_x2/fpc_hn | |
|---|---|---|---|---|---|---|---|---|---|
| 0.183 | B−K$\alpha$ | 0.94217 ± | 0.00321 | 0.80596 ± | 0.00279 | 0.84037 ± | 0.00291 | 0.79127 ± | 0.00365 |
| 0.277 | C−K$\alpha$ | 0.95889 ± | 0.00210 | 0.92793 ± | 0.00203 | 0.92887 ± | 0.00254 | 0.90116 ± | 0.00420 |
| 0.277 | C−K$\alpha$ | 0.95889 ± | 0.00210 | 0.92793 ± | 0.00203 | 0.92887 ± | 0.00254 | 0.90116 ± | 0.00420 |
| 0.524 | O−K$\alpha$ | ... ± | ... | 0.76078 ± | 0.00255 | 0.86475 ± | 0.00290 | 0.78077 ± | 0.00705 |
| 0.705 | Fe−L$\alpha$ | 0.97460 ± | 0.00307 | 0.84695 ± | 0.00241 | 0.88800 ± | 0.00252 | 0.86342 ± | 0.00404 |
| 0.852 | Ni−L$\alpha$ | 0.98044 ± | 0.00293 | 0.89929 ± | 0.00270 | 0.93605 ± | 0.00281 | 0.91379 ± | 0.00485 |
| 0.929 | Cu−L$\alpha$ | 0.98995 ± | 0.01601 | 0.94042 ± | 0.00241 | 0.96131 ± | 0.00247 | 0.96080 ± | 0.00525 |
| 1.254 | Mg−K$\alpha$ | 0.99443 ± | 0.00978 | 0.98062 ± | 0.00950 | 0.98062 ± | 0.00952 | 0.95801 ± | 0.00843 |
| 1.486 | Al−K$\alpha$ | ... ± | ... | 0.98271 ± | 0.01438 | 0.98350 ± | 0.01436 | 0.97405 ± | 0.01474 |
| 1.486 | Al−K$\alpha$ | 0.99326 ± | 0.00396 | 0.98358 ± | 0.00380 | 0.98488 ± | 0.00378 | 0.96829 ± | 0.00476 |
| 1.739 | Si−K$\alpha$ | ... ± | ... | 0.92961 ± | 0.00620 | 0.93868 ± | 0.00665 | 1.02899 ± | 0.00882 |
| 2.166 | Nb−L$\alpha$ | 0.98655 ± | 0.00491 | 0.99937 ± | 0.00477 | 0.98863 ± | 0.00473 | 0.99318 ± | 0.00596 |
| 2.980 | Ag−L$\alpha$ | 0.98689 ± | 0.00677 | 1.00136 ± | 0.00634 | 0.99062 ± | 0.00629 | 0.97519 ± | 0.00715 |
| 3.444 | Sn−L$\alpha$ | 0.99592 ± | 0.00640 | 0.99713 ± | 0.00585 | 1.00344 ± | 0.00588 | 0.96486 ± | 0.00669 |
| 4.510 | Ti−K$\alpha$ | ... ± | ... | 1.00306 ± | 0.00784 | 1.00241 ± | 0.00783 | 1.04596 ± | 0.00994 |
| 4.510 | Ti−K$\alpha$ | 0.96891 ± | 0.00468 | 1.00925 ± | 0.00461 | 0.98500 ± | 0.00455 | 0.94846 ± | 0.00572 |
| 5.410 | Cr−K$\alpha$ | 0.94797 ± | 0.00467 | 0.97872 ± | 0.00462 | 0.96246 ± | 0.00453 | 0.89659 ± | 0.00545 |
| 6.400 | Fe−K$\alpha$ | ... ± | ... | 0.94574 ± | 0.04193 | 0.95654 ± | 0.04243 | 1.25165 ± | 0.04361 |
| 6.400 | Fe−K$\alpha$ | 0.97052 ± | 0.00563 | 1.00101 ± | 0.00553 | 0.97457 ± | 0.00540 | 0.94306 ± | 0.00852 |
| 8.029 | Cu−K$\alpha$ | ... ± | ... | 1.04459 ± | 0.03147 | 1.05810 ± | 0.03188 | 1.62196 ± | 0.03159 |
| 8.620 | Zn−K$\alpha$ | 0.88706 ± | 0.00319 | 0.89029 ± | 0.00588 | 0.88850 ± | 0.00319 | 0.94848 ± | 0.00630 |

Table 3.5: Relative Quantum Efficiencies ($QE_{det}/QE_{\mathsf{fpc\_hn}}$) for the FPC detectors from Phases I & J XRCF flat field testing, corrected to 10° C





| E (keV) | Line | fpc_hb/fpc_5 | | ssd_5/fpc_5 | |
|---|---|---|---|---|---|
| 0.524 | O−K$\alpha$ | 1.46295 ± | 0.09260 | ... ± | ... |
| 1.486 | Al−K$\alpha$ | ... ± | ... | 0.83396 ± | 0.00956 |
| 1.739 | Si−K$\alpha$ | 1.01822 ± | 0.00582 | 0.92861 ± | 0.00473 |
| 2.166 | Nb−L$\alpha$ | ... ± | ... | 0.97837 ± | 0.00652 |
| 4.510 | Ti−K$\alpha$ | ... ± | ... | 0.99148 ± | 0.01325 |
| 6.400 | Fe−K$\alpha$ | ... ± | ... | 1.65221 ± | 0.00772 |
| 8.029 | Cu−K$\alpha$ | ... ± | ... | 2.46718 ± | 0.23668 |

Table 3.6: Relative Quantum Efficiencies ($QE_{det}/QE_{\mathsf{fpc\_5}}$) for the FPC detectors from Phase I XRCF flat field testing, corrected to 10° C

| E (keV) | Line | fpc_hb/fpc_x1 | | ssd_x/fpc_x1 | |
|---|---|---|---|---|---|
| 0.852 | Ni−L$\alpha$ | ... ± | ... | 0.28041 ± | 0.01517 |
| 1.254 | Mg−K$\alpha$ | 0.99237 ± | 0.00830 | 0.72842 ± | 0.00342 |
| 1.486 | Al−K$\alpha$ | 1.00035 ± | 0.00344 | 0.74572 ± | 0.00336 |
| 2.166 | Nb−L$\alpha$ | 1.02267 ± | 0.00399 | 0.90712 ± | 0.00428 |
| 2.980 | Ag−L$\alpha$ | 1.04323 ± | 0.00548 | 1.38284 ± | 0.00656 |
| 3.444 | Sn−L$\alpha$ | 0.99431 ± | 0.00590 | 0.88771 ± | 0.00498 |
| 4.510 | Ti−K$\alpha$ | 1.05040 ± | 0.00404 | 1.11598 ± | 0.00493 |
| 5.410 | Cr−K$\alpha$ | 1.02044 ± | 0.00437 | 1.27460 ± | 0.00573 |
| 6.400 | Fe−K$\alpha$ | 1.03022 ± | 0.00495 | 1.50606 ± | 0.00738 |
| 8.620 | Zn−K$\alpha$ | 1.03440 ± | 0.00423 | 2.98828 ± | 0.01148 |

Table 3.7: Relative Quantum Efficiencies ($QE_{det}/QE_{\mathsf{fpc\_x1}}$) for the FPC detectors from Phase J XRCF flat field testing, corrected to 10° C

| E (keV) | fpc_5/fpc_hn | |
|---|---|---|
| 0.183 | 0.96346 ± | 0.01125 |
| 0.276 | 0.98315 ± | 0.01000 |
| 0.705 | 0.91775 ± | 0.03536 |
| 1.254 | 1.00441 ± | 0.01479 |
| 1.487 | 1.01667 ± | 0.00930 |
| 2.290 | 1.01290 ± | 0.00929 |
| 2.980 | 1.01626 ± | 0.01283 |
| 4.510 | 1.04801 ± | 0.01443 |
| 6.400 | 1.03286 ± | 0.00767 |
| 8.030 | 0.99712 ± | 0.01351 |
| 8.030 | 1.04397 ± | 0.01486 |

Table 3.8: Relative Quantum Efficiencies ($QE_{\mathsf{fpc\_5}}/QE_{\mathsf{fpc\_hn}}$) for the FPC detectors from Beam Uniformity tests in Phases D and E XRCF testing, corrected to 10° C

### 3.5.4 Relating Flat Field, HRMA, and BESSY measurements

As noted in the introduction to the section on Quantum Efficiency, because of differences in gas temperature and how the FPCs were illuminated, certain adjustments must be made when applying one set of detector QE calibration results to another situation. Table 3.4 listed the differences among these situations, and §3.5.1 explained how window bowing and nonuniformity data were collected for fpc_hn and fpc_x2. In the following subsections we discuss how QE corrections for various effects are calculated and applied.

#### Window Absorption Corrections

As explained earlier, measurements of fpc_hn QE made on the BESSY SX700 monochromator are not directly applicable to the XRCF because only the center of the central windowlet of the FPC was absolutely calibrated. Nonuniformities in window thickness over the entire blocking plate aperture, as well as the effects of variable effective path length within each windowlet, must be considered when assigning a net QE to fpc_hn as it was used during AXAF and flat field calibration. The same considerations apply for fpc_x2 when analyzing flat field data, or when computing the effective QE when a HRMA-focussed image extends over more than just the center of one windowlet.

It is our intention to analyze the large- and small-scale QE mapping data for fpc_hn and fpc_x2 and develop tables of energy-dependent correction factors for each FPC, along the lines of the Gas Absorption Correction table described in the next subsubsection. As part of our analysis, and to guide the construction of a theoretical model, we will also use the results of Lester Cohen's finite-element modeling of FPC window deflections (Cohen, 1995), which was based on Dick Goddard's experimental measurements Goddard (1994).

#### Gas Absorption Corrections

There are three effects related to absorption of x-rays in the FPC gas which modify the detector QE: effective absorption path length, absorption of x-rays by the anode wire, and gas density (which depends on pressure and temperature). QE modifications for each of these effects for all relevant combinations of detector, aperture, and HRMA shell and quadrant were calculated using the `qegas.f` FORTRAN program (which is extensively documented and includes definitive FPC dimensions, such as a distance of 9.12 mm from HXDA aperture plane to deflected FPC window, and a gas depth of 55.02 mm with undeflected window—see Appendices for URLs) and are listed in Table 3.9 at the energies of relevant absorption edges and selected Penning source and EIPS characteristic emission lines. In the table, QE modifications are listed as percentage differences; a more complete table with over 550 energies is available which lists QE correction *factors*.

At each energy, the `QEref` column lists the QE of a model reference FPC, defined as a BND-H FPC with full rectangular aperture, no anode wire, average gas depth 55.93 mm, P10 gas with 90.01% Ar and 9.99% methane at 400 torr and 10 °C, with a 1.0-$\mu$m-thick, 1.3-g/cm$^3$ polyimide ($C_{22}H_{10}O_4N_2$) window and a 200-Å coating of 2.694-g/cm$^3$ aluminum. Other column headings will be explained below. The table should be used to determine *relative* QE corrections, such as when correcting for temperature differences, or applying the measured flat-field QE of fpc_x2 (relative to fpc_hn) to analyze data acquired during AXAF calibration with a focussed x-ray beam. As is obvious from the table, at low energies, where the gas is opaque, differences in the optical depth of the gas have no impact on QE.

As seen in Figure 3.15, the wire support grid deflects by approximately 1.25 mm in the center of the window, and the polyimide/Al window material bulges out another 0.25 mm between the wires





| Energy | OpDep | QEref | x2norm | 1ns | 1tb | 3ns | 3tb | 4ns | 4tb | 6ns | 6tb | hn36 | hfull | f5-36 | f5-12 | f5-4 | f5-1 | bessy | per-dC |
|---|---|---|---|---|---|---|---|---|---|---|---|---|---|---|---|---|---|---|---|
| 77.5 | 99.999 | 0.001 | 0.000 | 0.000 | 0.000 | 0.000 | 0.000 | 0.000 | 0.000 | 0.000 | 0.000 | 0.000 | 0.000 | 0.000 | 0.000 | 0.000 | 0.000 | 0.000 | 0.000 |
| 95.0 | 98.777 | 0.005 | 0.000 | 0.000 | 0.000 | 0.000 | 0.000 | 0.000 | 0.000 | 0.000 | 0.000 | 0.000 | 0.000 | 0.000 | 0.000 | 0.000 | 0.000 | 0.000 | 0.000 |
| 108.5 | 87.609 | 0.015 | 0.000 | 0.000 | 0.000 | 0.000 | 0.000 | 0.000 | 0.000 | 0.000 | 0.000 | 0.000 | 0.000 | 0.000 | 0.000 | 0.000 | 0.000 | 0.000 | 0.000 |
| 183.3 | 41.160 | 0.212 | 0.000 | 0.000 | 0.000 | 0.000 | 0.000 | 0.000 | 0.000 | 0.000 | 0.000 | 0.000 | 0.000 | 0.000 | 0.000 | 0.000 | 0.000 | 0.000 | 0.000 |
| 221.0 | 27.727 | 0.386 | 0.000 | 0.000 | 0.000 | 0.000 | 0.000 | 0.000 | 0.000 | 0.000 | 0.000 | 0.000 | 0.000 | 0.000 | 0.000 | 0.000 | 0.000 | 0.000 | 0.000 |
| 277.0 | 99.999 | 0.587 | 0.000 | 0.000 | 0.000 | 0.000 | 0.000 | 0.000 | 0.000 | 0.000 | 0.000 | 0.000 | 0.000 | 0.000 | 0.000 | 0.000 | 0.000 | 0.000 | 0.000 |
| 284.1 | 99.999 | 0.609 | 0.000 | 0.000 | 0.000 | 0.000 | 0.000 | 0.000 | 0.000 | 0.000 | 0.000 | 0.000 | 0.000 | 0.000 | 0.000 | 0.000 | 0.000 | 0.000 | 0.000 |
| 392.4 | 99.999 | 0.083 | 0.000 | 0.000 | 0.000 | 0.000 | 0.000 | 0.000 | 0.000 | 0.000 | 0.000 | 0.000 | 0.000 | 0.000 | 0.000 | 0.000 | 0.000 | 0.000 | 0.000 |
| 409.8 | 99.999 | 0.107 | 0.000 | 0.000 | 0.000 | 0.000 | 0.000 | 0.000 | 0.000 | 0.000 | 0.000 | 0.000 | 0.000 | 0.000 | 0.000 | 0.000 | 0.000 | 0.000 | 0.000 |
| 410.0 | 99.999 | 0.089 | 0.000 | 0.000 | 0.000 | 0.000 | 0.000 | 0.000 | 0.000 | 0.000 | 0.000 | 0.000 | 0.000 | 0.000 | 0.000 | 0.000 | 0.000 | 0.000 | 0.000 |
| 451.2 | 99.999 | 0.137 | 0.000 | 0.000 | 0.000 | 0.000 | 0.000 | 0.000 | 0.000 | 0.000 | 0.000 | 0.000 | 0.000 | 0.000 | 0.000 | 0.000 | 0.000 | 0.000 | 0.000 |
| 524.9 | 75.327 | 0.254 | 0.000 | 0.000 | 0.000 | 0.000 | 0.000 | 0.000 | 0.000 | 0.000 | 0.000 | 0.000 | 0.000 | 0.000 | 0.000 | 0.000 | 0.000 | 0.000 | 0.000 |
| 543.1 | 70.017 | 0.284 | 0.000 | 0.000 | 0.000 | 0.000 | 0.000 | 0.000 | 0.000 | 0.000 | 0.000 | 0.000 | 0.000 | 0.000 | 0.000 | 0.000 | 0.000 | 0.000 | 0.000 |
| 543.2 | 69.960 | 0.179 | 0.000 | 0.000 | 0.000 | 0.000 | 0.000 | 0.000 | 0.000 | 0.000 | 0.000 | 0.000 | 0.000 | 0.000 | 0.000 | 0.000 | 0.000 | 0.000 | 0.000 |
| 572.8 | 61.929 | 0.222 | 0.000 | 0.000 | 0.000 | 0.000 | 0.000 | 0.000 | 0.000 | 0.000 | 0.000 | 0.000 | 0.000 | 0.000 | 0.000 | 0.000 | 0.000 | 0.000 | 0.000 |
| 676.8 | 41.670 | 0.372 | 0.000 | 0.000 | 0.000 | 0.000 | 0.000 | 0.000 | 0.000 | 0.000 | 0.000 | 0.000 | 0.000 | 0.000 | 0.000 | 0.000 | 0.000 | 0.000 | 0.000 |
| 705.0 | 37.977 | 0.408 | 0.000 | 0.000 | 0.000 | 0.000 | 0.000 | 0.000 | 0.000 | 0.000 | 0.000 | 0.000 | 0.000 | 0.000 | 0.000 | 0.000 | 0.000 | 0.000 | 0.000 |
| 851.5 | 23.619 | 0.581 | 0.000 | 0.000 | 0.000 | 0.000 | 0.000 | 0.000 | 0.000 | 0.000 | 0.000 | 0.000 | 0.000 | 0.000 | 0.000 | 0.000 | 0.000 | 0.000 | 0.000 |
| 929.7 | 18.846 | 0.651 | 0.000 | 0.000 | 0.000 | 0.000 | 0.000 | 0.000 | 0.000 | 0.000 | 0.000 | 0.000 | 0.000 | 0.000 | 0.000 | 0.000 | 0.000 | 0.000 | 0.000 |
| 1011.7 | 15.113 | 0.711 | 0.000 | 0.000 | 0.000 | 0.000 | 0.000 | 0.000 | 0.000 | 0.000 | −.001 | 0.000 | 0.000 | 0.000 | 0.000 | 0.000 | 0.000 | 0.000 | 0.000 |
| 1253.6 | 8.550 | 0.828 | −.005 | 0.002 | −.010 | 0.002 | −.013 | 0.002 | −.015 | 0.002 | −.020 | −.005 | −.001 | −.005 | 0.000 | −.001 | −.001 | 0.002 | −.001 |
| 1486.7 | 5.385 | 0.886 | −.021 | 0.030 | −.034 | 0.028 | −.050 | 0.028 | −.061 | 0.027 | −.093 | −.021 | −.007 | −.021 | −.003 | −.013 | −.017 | 0.025 | −.009 |
| 1559.5 | 4.750 | 0.895 | −.026 | 0.050 | −.038 | 0.047 | −.061 | 0.046 | −.077 | 0.045 | −.120 | −.027 | −.010 | −.027 | −.005 | −.022 | −.028 | 0.043 | −.014 |
| 1559.7 | 4.749 | 0.877 | −.026 | 0.050 | −.038 | 0.047 | −.061 | 0.046 | −.077 | 0.045 | −.120 | −.027 | −.010 | −.027 | −.005 | −.022 | −.028 | 0.043 | −.014 |
| 1740.0 | 3.567 | 0.888 | −.037 | 0.125 | −.030 | 0.119 | −.074 | 0.116 | −.103 | 0.112 | −.181 | −.038 | −.017 | −.038 | −.013 | −.054 | −.069 | 0.107 | −.035 |
| 1775.0 | 3.385 | 0.887 | −.038 | 0.143 | −.026 | 0.136 | −.074 | 0.133 | −.105 | 0.129 | −.191 | −.040 | −.019 | −.040 | −.015 | −.062 | −.079 | 0.123 | −.041 |
| 2042.4 | 2.335 | 0.853 | −.041 | 0.304 | 0.034 | 0.289 | −.046 | 0.283 | −.097 | 0.273 | −.237 | −.044 | −.030 | −.044 | −.031 | −.131 | −.167 | 0.261 | −.085 |
| 2165.9 | 1.996 | 0.823 | −.039 | 0.382 | 0.072 | 0.363 | −.022 | 0.355 | −.082 | 0.343 | −.243 | −.042 | −.034 | −.042 | −.039 | −.164 | −.209 | 0.328 | −.107 |
| 2293.2 | 1.711 | 0.786 | −.036 | 0.460 | 0.113 | 0.437 | 0.006 | 0.428 | −.061 | 0.413 | −.243 | −.039 | −.038 | −.039 | −.047 | −.197 | −.251 | 0.394 | −.129 |
| 2984.3 | 0.827 | 0.552 | −.010 | 0.788 | 0.309 | 0.748 | 0.154 | 0.732 | 0.059 | 0.707 | −.196 | −.014 | −.052 | −.014 | −.081 | −.334 | −.427 | 0.675 | −.219 |
| 3205.8 | 0.674 | 0.482 | −.003 | 0.860 | 0.356 | 0.816 | 0.192 | 0.799 | 0.090 | 0.771 | −.179 | −.007 | −.054 | −.007 | −.088 | −.364 | −.465 | 0.737 | −.238 |
| 3206.0 | 6.363 | 0.983 | −.014 | 0.013 | −.025 | 0.012 | −.035 | 0.012 | −.041 | 0.012 | −.060 | −.014 | −.004 | −.014 | −.001 | −.006 | −.007 | 0.011 | −.004 |
| 3444.0 | 5.323 | 0.983 | −.021 | 0.031 | −.034 | 0.030 | −.051 | 0.029 | −.063 | 0.028 | −.095 | −.022 | −.007 | −.022 | −.003 | −.014 | −.018 | 0.027 | −.009 |
| 4510.8 | 2.644 | 0.924 | −.042 | 0.245 | 0.009 | 0.233 | −.060 | 0.228 | −.105 | 0.220 | −.226 | −.044 | −.026 | −.044 | −.025 | −.106 | −.135 | 0.210 | −.069 |
| 5414.7 | 1.617 | 0.799 | −.034 | 0.489 | 0.128 | 0.464 | 0.017 | 0.454 | −.053 | 0.438 | −.242 | −.037 | −.039 | −.037 | −.050 | −.209 | −.266 | 0.419 | −.137 |
| 5898.8 | 1.279 | 0.720 | −.026 | 0.603 | 0.194 | 0.573 | 0.066 | 0.560 | −.015 | 0.541 | −.230 | −.030 | −.044 | −.030 | −.062 | −.257 | −.328 | 0.517 | −.168 |
| 6403.8 | 1.019 | 0.638 | −.018 | 0.704 | 0.256 | 0.669 | 0.113 | 0.655 | 0.024 | 0.632 | −.214 | −.022 | −.049 | −.022 | −.072 | −.299 | −.382 | 0.604 | −.196 |
| 6930.3 | 0.818 | 0.558 | −.010 | 0.792 | 0.312 | 0.752 | 0.156 | 0.736 | 0.060 | 0.710 | −.195 | −.014 | −.052 | −.014 | −.081 | −.336 | −.429 | 0.679 | −.220 |
| 7478.1 | 0.661 | 0.483 | −.002 | 0.866 | 0.360 | 0.822 | 0.195 | 0.804 | 0.093 | 0.776 | −.178 | −.007 | −.055 | −.007 | −.088 | −.366 | −.468 | 0.742 | −.240 |
| 8047.8 | 0.538 | 0.416 | 0.004 | 0.927 | 0.401 | 0.880 | 0.228 | 0.861 | 0.121 | 0.831 | −.161 | 0.000 | −.057 | 0.000 | −.095 | −.392 | −.500 | 0.794 | −.257 |
| 8397.6 | 0.477 | 0.379 | 0.008 | 0.959 | 0.422 | 0.910 | 0.245 | 0.891 | 0.136 | 0.860 | −.152 | 0.003 | −.058 | 0.003 | −.098 | −.405 | −.517 | 0.821 | −.265 |
| 8638.9 | 0.440 | 0.356 | 0.010 | 0.978 | 0.435 | 0.929 | 0.256 | 0.909 | 0.145 | 0.877 | −.146 | 0.005 | −.058 | 0.005 | −.100 | −.413 | −.527 | 0.838 | −.271 |
| 9672.3 | 0.319 | 0.273 | 0.017 | 1.044 | 0.480 | 0.991 | 0.293 | 0.970 | 0.178 | 0.936 | −.126 | 0.012 | −.061 | 0.012 | −.106 | −.441 | −.562 | 0.894 | −.289 |

Table 3.9: QE Corrections for gas opacity effects. `QEref` is the QE of the reference detector, defined as fpc_hn with full aperture and no anode absorption at 400 torr and 10 °C, with average window deflection of 0.91 mm. All columns except the first two represent the percentage change in QE relative to the reference FPC. As an example, at Cu-K, `bessy` = 0.794 and `x2norm` = 0.004, so the QE of fpc_x2 as measured at BESSY (where the center of a slightly off-center windowlet—to avoid anode wire absorption—was exposed to normal incidence x-rays) is 0.790% higher than its effective QE during flat field testing (where the entire blocking plate aperture was exposed) because of differences in effective gas depth and anode wire absorption.

within each 2-mm-square windowlet. Because of this window deflection and the fact that HRMA-focussed x-rays intercept the focal plane FPC window at its point of maximum deflection, the gas depth is about 0.6 mm longer in fpc_x2 than the the average gas depth for the BND-H FPCs. Average deflections for window areas which are exposed to x-rays with various combinations of detector and aperture range from 0.54 mm (for fpc_5 with its 1-mm aperture) to 1.50 mm (for any FPC exposed in the center of its window). (Some refinement in window deflection values will occur once Lester Cohen's window deflection model has been studied.) QE adjustments for each of these x-ray exposure combinations are listed in Table 3.9, with the `x2norm` column referring to fpc_x2 with its 36.784-mm blocking plate aperture during flat-field normal-incidence calibration, `hfull` to BND-H FPCs with their rectangular apertures, `bessy` to fpc_hn or fpc_x2 at BESSY, `f5_36` to fpc_5 with its 36-mm aperture, and so on.

There are eight columns that apply to fpc_x2 when exposed to focussed beams, with North & South and Top & Bottom quadrants for each of the four HRMA shells. The breakdown by shell is needed because the effective gas depth along the focussed rays is increased by a factor of the secant of the angle of incidence, which adds another 0.1 mm for x-rays focussed by HRMA shell 1 (with cone half-angle equal to 3.3873°) and less for the other shells. At high energies where opacity approaches zero, this net ∼1.2% increase in gas depth (0.6 mm plus 0.1 mm out of about 56 mm) relative to the BND-H FPCs leads to a similar relative increase in QE, as shown in column `1ns`, for instance 0.8% at Ag-$L\alpha$ (just below the Ar-K edge), and 0.9% at Cu-$K\alpha$.

The further breakdown by quadrants is necessary because of anode absorption, which occurs when x-rays strike the anode wire running down the middle of the FPC. Instead of ionizing a gas atom which leads to an electron avalanche, the absorbed x-ray produces a very small electrical signal which may or may not appear as a weak feature at very low channels, and so that event is effectively lost.

Anode absorption occurs whenever the gas is not opaque and x-rays are directed toward the 50-$\mu$m-diameter anode wire. It *does not* occur, therefore, when the 1-, 4-, or 12-mm apertures are used with fpc_5 (since they are offset to one side of the window), or for x-rays collected by any of the North or South quadrants of the HRMA (since those x-rays are focussed into quarter-cones which intercept the vertically oriented fpc_x2 to either side of its anode wire). The largest quadrant-specific differences occur for shell 6, which has the smallest-diameter x-ray cone and therefore the largest fraction of x-rays aimed at the anode wire. At Cu-K, the relative difference in QE is 1.0%, from $QE_{6ns}/QE_{6tb} = (1 + 0.0083)/(1 - 0.0016) = 1.010$. When analyzing spectra acquired using a full shell, simply average the NS and TB columns. When analyzing spectra from more than one shell, use an effective-area-weighted average of the appropriate columns.

In most cases, the largest QE adjustments needed to relate one set of calibration results to another arise from differences in gas density, which is proportional to pressure and inversely proportional to temperature (in Kelvins). Because all the BND-H and focal plane FPCs were run off the same gas supply system, the pressure was virtually identical for all of them (and stable at 400 torr to within ∼0.1 torr). Temperature differences, however, of 10 or more degrees were not uncommon between different FPCs or calibration periods (see Table 3.4).

Percentage changes per degree Celsius (or Kelvin) are listed in the `per_dC` column and range up to nearly 0.3% per degree at 10 keV. Those correction terms, however, are strictly applicable only for small differences (a few degrees), and are shown merely for illustrative purposes. Proper corrections use the `OpDepth` column, which lists the optical depth of the gas at each energy, equal to $\sum \mu\rho l$, assuming 90.01% Ar and 9.99% methane at 10 °C and 400 torr. The ratio of QEs of a





single FPC at two different temperatures is then given by

$$\frac{QE(T_1)}{QE(T_2)} = \frac{1 - e^{-OpDepth(273.15+T_0)/(273.15+T_1)}}{1 - e^{-OpDepth(273.15+T_0)/(273.15+T_2)}}$$

where all the temperatures are in degrees Celsius and $T_0$ is the reference temperature of 10 °C.

(To date, none of these gas depth and anode absorption corrections have been applied to data analysis results because they are so small.)

Gas temperature corrections can be significant and have been applied to all flat field and (where necessary) BESSY data. The gas depth and anode absorption corrections, by comparison, are almost negligible, and have not been applied to any results. In the interest of thoroughness, however, the largest uncertainty in the gas depth/anode absorption corrections arises from the average window deflection, and the critical term there is the difference between the average fpc_x2 deflection and the central windowlet deflection. This is conservatively estimated this to be 0.42 ± 0.15 mm, resulting in an error of less than 0.22% at 10 keV.

**Off-Axis and Grating Measurements**

All the gas opacity corrections discussed thus far apply only to normal incidence or on-axis focussed x-rays. QE corrections for off-axis and grating measurements will be somewhat different for fpc_x2 because the images will in general extend across more than just the center of one windowlet (particularly for grating-dispersed intrinsically broad lines), but such correction factors will generally differ from the on-axis factors by no more than one percent, and so it should suffice to use rough approximations of the average angle of incidence and the image location with respect to the center of the central windowlet.

Corrections for variable window transmission and obscuration by window support wires will generally be larger and thus more difficult to estimate. As noted earlier, however, none of the window bowing and nonuniformity data have yet been analyzed.

### 3.5.5 Final Results: Standardized FPC QEs

This subsection describes the calculation of absolute quantum efficiencies for the BND-H detectors and the fpc_x2. We outline here the steps used in deriving these tables, and point out the possible systematic effects remaining in these data.

There are two energy regimes, $E < 1.700$ keV, and $E > 1.700$ keV.

For $E < 1.700$ keV, we have absolute calibrations for the fpc_hn and fpc_x2 from the SX700 beamline at BESSY. Details are in Auerhammer et al. (1998). The data were reduced as in §3.5.1, and combined with beam current files tabulated by J. Auerhammer.

For $E > 1.700$ keV, we have currently no absolute standard. We therefore have used a theoretical SSD QE curve, presuming the QE of an SSD is just the window transmission, using 2000 Angstroms of aluminum plus 1.25 microns of Parylene ($C_8H_8$, density 1.1 g cm$^{-3}$, and Henke tables from 1995. When results from the BESSY calibration of the SSD detectors are available, they will be incorporated.

Relative quantum efficiencies were measured in Phases I and J at XRCF, in two kinds of experiments: BND-500 maps and BND-H maps. These data and their reduction are described in §3.5.3.

The BND-500 maps exposed the fpc_5 at its home position, the ssd_5 position, and the projected position of the fpc_hb. When the shutters were open (all of phase J, and a few tests in phase I),

this allows relative QE to be computed for these 3 detectors, correcting for beam uniformity and temperature effects (for the FPCs).

The Phase I and J BND-H maps exposed the fpc_hn at its home position, the positions of the other fpc_h detectors, and the (projected) position of the fpc_x2. Relative QE's for these detectors were then computed at these energies, including BU and T corrections.

All QE's and relative QE's for FPC detectors are temperature corrected to 10°C.

We also have a code that allows us to fit a model of the form:

- a slab of Al
- a slab of polyimide ($C_{22}H_{10}O_4N_2$, density 1.33)
- a box of gas (P-10 = 90% Ar + 10% $CH_4$)
- an energy-independent geometrical factor

to a QE curve. We have done this with the BESSY SX700 data for fpc_hn and fpc_x2. We find recent Henke tables unable to adequately fit the data, so we fit them in energy slices, allowing different window thicknesses to make up for the inadequate Henke data. It may be the case that the stoichiometry of the plastic is slightly different from the above, or that older (or newer) Henke tables would do a better job of fitting these data.

To summarize, we obtain the QE of detectors in the following manner:

- For $E < 1700$ eV: interpolate the SX700 data with Henke fits for fpc_x2 and fpc_hn. Use RQE from phase I & J BND-H maps to get other fpc_h QEs at selected energies. Interpolate between these points to get QE(fpc_h*,E).
- For $E > 1700$ eV: Using the theoretical SSD QE curve, BND-500 maps allow computation of the QE of fpc_hb and fpc_5 (phase I),or fpc_x1, (phase J) at selected energies. Then the contemporary BND-H maps allow computation of other fpc_h QE from the fpc_hb numbers. We then interpolate between these points to get QE(fpc_h*,E).

To obtain fits for the other fpc_h detectors, we allow only the window thickness to vary, providing a single free parameter (the ratio of the detector's window thickness to the fitted value for fpc_hn). We require the same thickness ratio in all energy slices, despite the need for different thickness values for the fpc_hn fit for each energy slice.

The results of these procedures are illustrated in Figures 3.20through3.22. Note especially in the fpc_hn and fpc_x2 plots (Figure 3.20) how poorly the fit to the Henke tables approximates the data. Still, the fit falls within 3% of all the points except those near edges (which have been excluded from the fits), and so represents a reasonably good way to interpolate between the sparse points where data exist for the other detectors.

We list the measured QE values for the fpc_hn and fpc_x2 in Table 3.10. We include those for the other fpc_h detectors in Table 3.11.

The fpc_5 is a slightly different case. We have obtained relative QE numbers for this detector from beam uniformity tests in phases D and E of the XRCF testing, by comparing fluxes taken simultaneously by the two detectors during BND-H maps, and correcting for beam uniformity effects based on data from a nearly contemporaneous BND-500 map. These relative QE numbers, corrected to 10°C, are presented in Table 3.8. Using these numbers and the absolute QE curve for the fpc_hn presented above, we can obtain an absolute QE curve for the fpc_5. The resulting curve is in Figure 3.23. The absolute QE numbers for fpc_5 are presented in Table 3.12.





Table 3.10: Absolute QE for fpc_x2 and fpc_hn.

| energy | QE(fpc_x2) | QE(fpc_hn) |
|---|---|---|
| 0.095 | 0.00239 ± 0.00003 | 0.00553 ± 0.00006 |
| 0.100 | 0.00423 ± 0.00005 | 0.00896 ± 0.00009 |
| 0.105 | 0.00689 ± 0.00007 | 0.01325 ± 0.00014 |
| 0.110 | 0.01001 ± 0.00011 | 0.01837 ± 0.00019 |
| 0.115 | 0.01559 ± 0.00017 | 0.02649 ± 0.00028 |
| 0.150 | 0.08014 ± 0.00085 | 0.11185 ± 0.00116 |
| 0.183 | 0.17972 ± 0.00190 | 0.22559 ± 0.00236 |
| 0.210 | 0.25883 ± 0.00340 | 0.30902 ± 0.00402 |
| 0.254 | 0.44066 ± 0.00349 | 0.49017 ± 0.00385 |
| 0.256 | 0.44667 ± 0.00353 | 0.49463 ± 0.00389 |
| 0.258 | 0.44866 ± 0.00354 | 0.49640 ± 0.00389 |
| 0.261 | 0.46432 ± 0.00462 | 0.51457 ± 0.00510 |
| 0.264 | 0.47175 ± 0.00609 | 0.52187 ± 0.00671 |
| 0.267 | 0.48475 ± 0.00974 | 0.53432 ± 0.01069 |
| 0.270 | 0.49778 ± 0.01336 | 0.54700 ± 0.01463 |
| 0.273 | 0.49754 ± 0.01581 | 0.54752 ± 0.01734 |
| 0.276 | 0.50911 ± 0.02642 | 0.55915 ± 0.02892 |
| 0.280 | 0.50242 ± 0.05257 | 0.55213 ± 0.05748 |
| 0.284 | 0.43048 ± 0.03710 | 0.47595 ± 0.04069 |
| 0.288 | 0.01317 ± 0.00117 | 0.01680 ± 0.00147 |
| 0.292 | 0.03013 ± 0.00275 | 0.03451 ± 0.00311 |
| 0.296 | 0.00587 ± 0.00035 | 0.00697 ± 0.00041 |
| 0.300 | 0.00122 ± 0.00007 | 0.00165 ± 0.00010 |
| 0.305 | 0.00054 ± 0.00003 | 0.00088 ± 0.00005 |
| 0.310 | 0.00204 ± 0.00013 | 0.00410 ± 0.00025 |
| 0.330 | 0.01043 ± 0.00017 | 0.01817 ± 0.00028 |
| 0.389 | 0.04270 ± 0.00039 | 0.06323 ± 0.00057 |
| 0.392 | 0.04514 ± 0.00040 | 0.06648 ± 0.00057 |
| 0.395 | 0.04763 ± 0.00042 | 0.06949 ± 0.00060 |
| 0.400 | 0.05162 ± 0.00045 | 0.07466 ± 0.00064 |
| 0.405 | 0.03828 ± 0.00033 | 0.05722 ± 0.00049 |
| 0.410 | 0.02656 ± 0.00023 | 0.04201 ± 0.00036 |
| 0.415 | 0.03854 ± 0.00034 | 0.05751 ± 0.00049 |
| 0.420 | 0.04785 ± 0.00040 | 0.06991 ± 0.00058 |
| 0.515 | 0.16761 ± 0.00139 | 0.21002 ± 0.00172 |
| 0.520 | 0.17520 ± 0.00145 | 0.21823 ± 0.00178 |
| 0.525 | 0.18157 ± 0.00150 | 0.22510 ± 0.00184 |
| 0.530 | 0.18470 ± 0.00150 | 0.22869 ± 0.00184 |
| 0.535 | 0.14927 ± 0.00122 | 0.18719 ± 0.00151 |
| 0.540 | 0.07835 ± 0.00064 | 0.10683 ± 0.00086 |
| 0.545 | 0.09211 ± 0.00076 | 0.12222 ± 0.00099 |
| 0.550 | 0.10633 ± 0.00087 | 0.13939 ± 0.00114 |
| 0.610 | 0.20106 ± 0.00161 | 0.24339 ± 0.00195 |
| 0.705 | 0.32485 ± 0.00255 | 0.37165 ± 0.00289 |

Table 3.10: Absolute QE for fpc_x2 and fpc_hn (continued)

| energy | QE(fpc_x2) | | QE(fpc_hn) | |
|---|---|---|---|---|
| 0.852 | 0.48896 ± | 0.00449 | 0.52912 ± | 0.00484 |
| 0.930 | 0.55858 ± | 0.00509 | 0.59247 ± | 0.00538 |
| 1.012 | 0.63479 ± | 0.00578 | 0.66650 ± | 0.00605 |
| 1.254 | 0.77416 ± | 0.00978 | 0.78901 ± | 0.00995 |
| 1.487 | 0.84923 ± | 0.01298 | 0.85279 ± | 0.01302 |
| 1.540 | 0.87167 ± | 0.01749 | 0.87613 ± | 0.01757 |
| 1.550 | 0.86902 ± | 0.01744 | 0.87424 ± | 0.01753 |
| 1.560 | 0.87456 ± | 0.01755 | 0.87641 ± | 0.01758 |
| 1.570 | 0.85495 ± | 0.01716 | 0.86390 ± | 0.01734 |
| 1.580 | 0.85931 ± | 0.01782 | 0.86522 ± | 0.01794 |
| 1.590 | 0.86201 ± | 0.01877 | 0.86694 ± | 0.01888 |
| 1.600 | 0.86649 ± | 0.02043 | 0.86795 ± | 0.02047 |
| 1.700 | 0.86248 ± | 0.02086 | 0.86759 ± | 0.02098 |
| 4.510 | 0.90130 ± | 0.01285 | 0.92300 ± | 0.00922 |
| 4.510 | 0.89122 ± | 0.00875 | 0.93957 ± | 0.00728 |
| 5.410 | 0.73849 ± | 0.00806 | 0.82354 ± | 0.00747 |
| 6.400 | 0.69454 ± | 0.04425 | 0.69761 ± | 0.00799 |
| 6.400 | 0.65795 ± | 0.00960 | 0.71063 ± | 0.03231 |
| 8.620 | 0.36862 ± | 0.00659 | 0.38860 ± | 0.00645 |

## 3.6 Future Work

Because so much FPC calibration data has only recently been acquired, a great deal of analysis remains to be finished. Substantial improvements can also be derived from the flat field calibration data, particularly at high energies, given more time. Below is a summary of work that remains.

**General**

- Spectral fitting accuracy can be improved by using the delta function plus top hat gain distribution for the BND-H FPCs (but not fpc_5, fpc_x2, or fpc_hn with its 36-mm aperture), letting the escape peak energy float a little (because of energy nonlinearities), using updated (and temperature-adjusted?) QE curves for each FPC, etc.
- The fraction of line counts arising from continuum escape is different between the BNDs and fpc_x2; corrections should be made, particularly for L-shell EIPS lines, which have relatively low line/continuum ratios.
- Corrections for gas temperature, window bowing, and focal plane image size should be automatically included in all analysis.
- Energy nonlinearity, particularly across the Ar-L edge, is not included in `JMKmod`. This may significantly affect the accuracy of low-energy fits, particularly for C-K where the below-edge and above-edge continua have different effective gains.
- None of the counting rate linearity data from BESSY have been analyzed. If there are significant errors at high rates, many measurements would be affected, particularly for fpc_x2 which was exposed to higher-intensity concentrated x-rays.





| E (keV) | QE(fpc_hs) | | QE(fpc_ht) | | QE(fpc_hb) | |
|---|---|---|---|---|---|---|
| 0.183 | 0.22589 ± | 0.00082 | 0.19324 ± | 0.00071 | 0.20149 ± | 0.00074 |
| 0.277 | 0.54843 ± | 0.00142 | 0.53072 ± | 0.00137 | 0.53126 ± | 0.00163 |
| 0.524 | ... ± | ... | 0.18166 ± | 0.00065 | 0.20655 ± | 0.00074 |
| 0.705 | 0.35661 ± | 0.00124 | 0.32766 ± | 0.00105 | 0.34354 ± | 0.00110 |
| 0.705 | 0.37704 ± | 0.00132 | 0.30991 ± | 0.00100 | 0.32493 ± | 0.00104 |
| 0.852 | 0.53155 ± | 0.00179 | 0.48755 ± | 0.00165 | 0.50749 ± | 0.00171 |
| 0.929 | 0.59796 ± | 0.00971 | 0.56805 ± | 0.00167 | 0.58067 ± | 0.00171 |
| 1.254 | 0.79132 ± | 0.00791 | 0.78033 ± | 0.00768 | 0.78034 ± | 0.00770 |
| 1.486 | ... ± | ... | 0.84251 ± | 0.01240 | 0.84319 ± | 0.01239 |
| 1.486 | 0.85158 ± | 0.00366 | 0.84329 ± | 0.00353 | 0.84439 ± | 0.00351 |
| 4.510 | ... ± | ... | 0.92708 ± | 0.01175 | 0.92651 ± | 0.00575 |
| 4.510 | 0.91135 ± | 0.00831 | 0.94936 ± | 0.00853 | 0.92651 ± | 0.00575 |
| 5.410 | 0.78163 ± | 0.00806 | 0.80703 ± | 0.00825 | 0.79358 ± | 0.00614 |
| 6.400 | ... ± | ... | 0.67276 ± | 0.04272 | 0.68054 ± | 0.00682 |
| 6.400 | 0.67771 ± | 0.00870 | 0.69902 ± | 0.00888 | 0.68054 ± | 0.00682 |
| 8.620 | 0.34490 ± | 0.00585 | 0.34616 ± | 0.00618 | 0.34546 ± | 0.00559 |

Table 3.11: Absolute Quantum Efficiencies for the fpc_ht, fpc_hb and fpc_hs detectors from XRCF flatfield measurements normalized to fpc_hn (up to 1.700 keV) and normalized to a theoretical SSD (above 1.700 keV), corrected to 10° C.

| energy | QE(fpc_5) | |
|---|---|---|
| 0.183 | 0.21735 ± | 0.00341 |
| 0.276 | 0.54973 ± | 0.02898 |
| 0.705 | 0.34108 ± | 0.01341 |
| 1.254 | 0.79241 ± | 0.01537 |
| 1.487 | 0.86579 ± | 0.01542 |
| 1.487 | 0.86252 ± | 0.01537 |
| 4.510 | 0.94466 ± | 0.01179 |
| 6.400 | 0.67726 ± | 0.01221 |

Table 3.12: Absolute Quantum Efficiencies for the fpc_5 detector from XRCF Phase D & E beam uniformity tests normalized to the fpc_hn, corrected to 10° C.

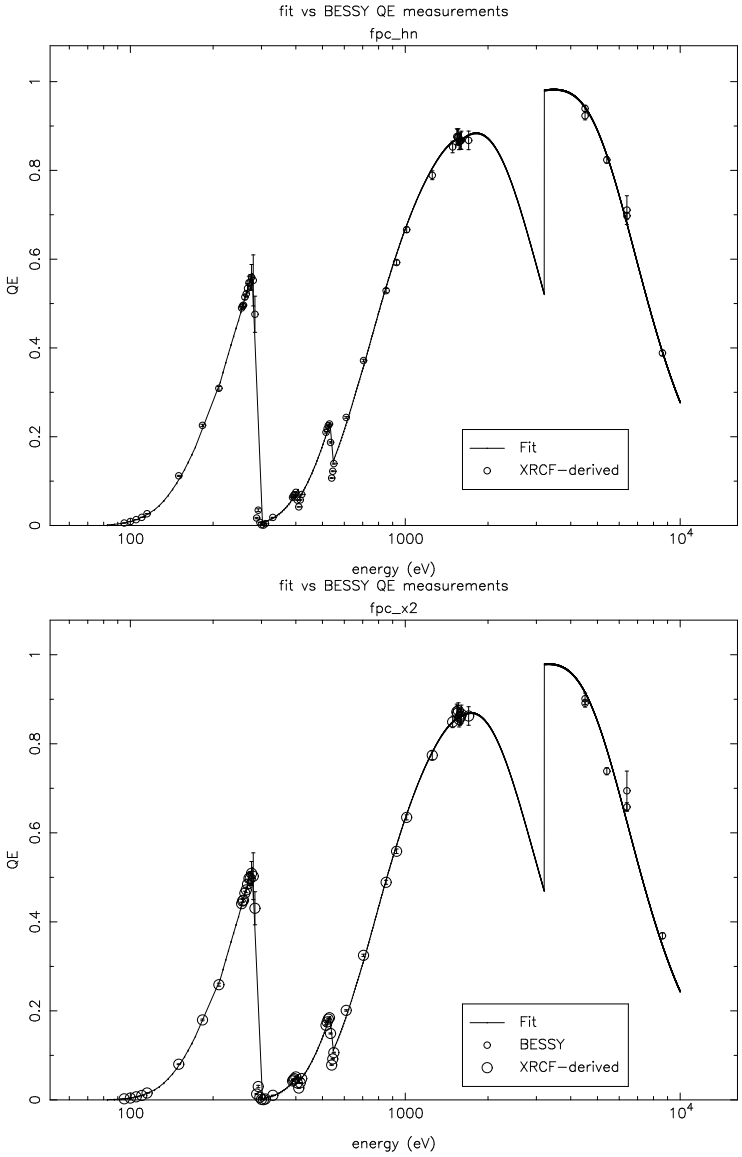


Figure 3.20: Absolute quantum efficiency for fpc_hn (top) and fpc_x2 from JMKmod fits to BESSY SX700 monochromator data ($E < 1.7$keV) and derived from a theoretical SSD curve and flatfield data ($E > 1.7$keV), with the fits described in the text.





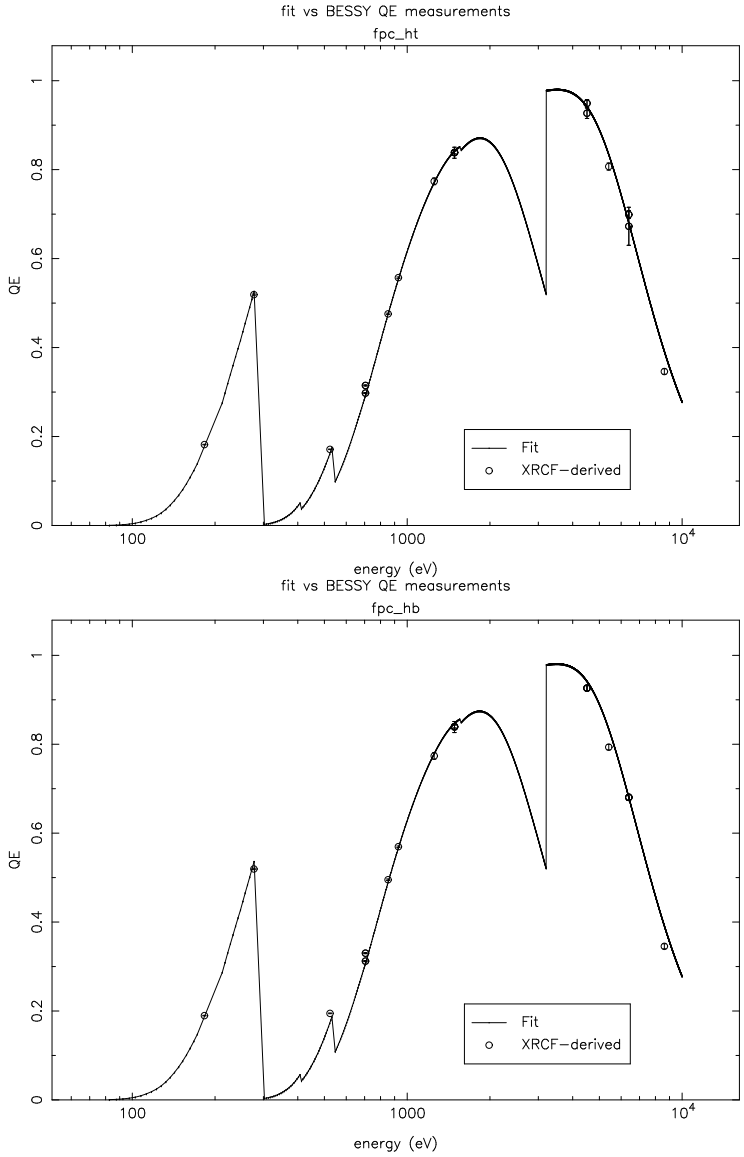


Figure 3.21: Absolute quantum efficiency for fpc_ht (top) and fpc_hb from flatfield data and the fpc_hn BESSY data ($E < 1.7$keV), and derived from a theoretical SSD curve and flatfield data ($E > 1.7$keV), with the fits described in the text.

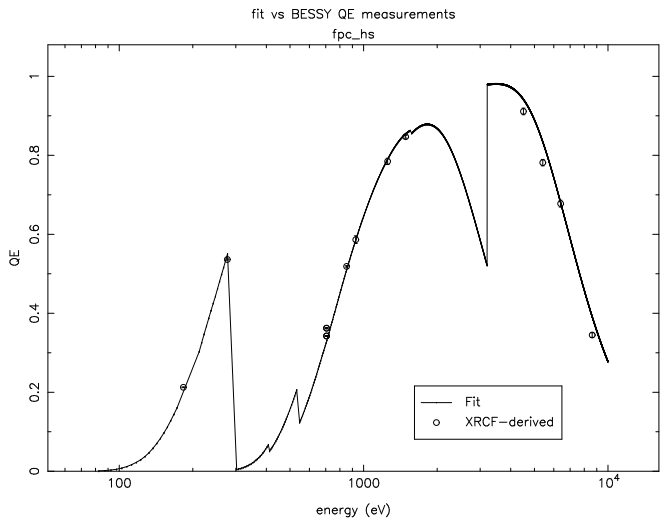


Figure 3.22: Absolute quantum efficiency for fpc_hs from flatfield data and the fpc_hn BESSY data ($E < 1.7$keV), and derived from a theoretical SSD curve and flatfield data ($E > 1.7$keV), with the fits described in the text.

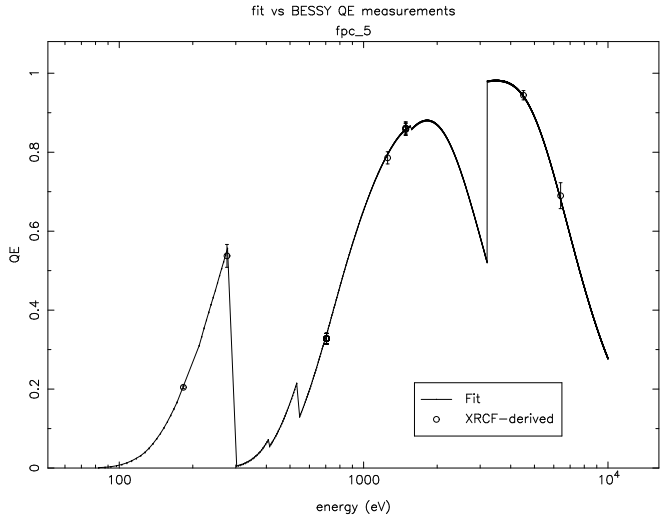


Figure 3.23: Absolute quantum efficiency for the fpc_5, derived from the fpc_hn curve and beam uniformity measurements in Phases D and E.





- Only half of the SSD deadtime consistency data (see Chapter 5) have been analyzed, and that was without applying the (small) corrections for incomplete pileup rejection that have been recently worked out.

**Flat Field Calibrations**

- None of the flat field data from November 1996 have been analyzed, apart from some preliminary FPC vs. HSI QE calibration. Good statistics were obtained with both SSDs (with ssd_x in the HXDA).
- Flat field data were collected at 19 energies (some of them during all three flat field calibration phases), but several of those energies have not yet been analyzed.
- Better statistics can be obtained for the beam uniformity maps by including more detectors for normalization, and by using *all* iterations at a given location.
- Much better statistics can be obtained for the relative counting rates of all BNDs by summing spectra from all the AXAF calibration runs at a given energy (as long as the source intensity and spectral shape are constant at the few percent level).
- Relatively less work has been done on the QE of fpc_5. Flat field data can also be used to calibrate the sizes of its four apertures.
- SSD data analysis is still relatively inaccurate at energies below 2 keV because of a lack of pileup rejection, but analysis tools to account for this are nearly ready. Improved FPC QEs can then be obtained at high energy via relative QE calibration.
- FPC spectral fitting accuracy can be checked by analyzing data taken at three energies with 2 and 4 mean-free-path source filters, and comparing the relative rates obtained with ssd_5 and the FPCs. The SSD analysis should be quite accurate because of its excellent energy resolution.

**BESSY SX700 QEs**

- Measured QEs are not always consistent (e.g., 705 eV), and there are sometimes jumps when the monochromator filter is changed.
- Why is the transmission of the fpc_x2 window so much higher than the net QE of the assembled detector? We are consulting with experts.
- Ring current logs must be edited to remove or correct occasional small (but sometimes extended) blips which can cause QE normalization errors. There may also be unexpected timestamp differences between BESSY and HXDS files.

**BESSY window mapping**

- None of these data have been analyzed.
- Results are needed to relate flat field and BESSY single-windowlet QEs, and to adjust the effective fpc_x2 QE when HRMA images are extended, as for off-axis and grating measurements.

**BESSY white beam**

- PTB has done some preliminary analysis, but results disagree with theoretical models by tens of percent below 1 keV.

- Analysis at low energies may be prohibitively difficult, but useful QE information can be derived for fpc_x2 and fpc_hn near the Ar-K edge for at least two of the filter combinations.